**Department of Physics and Astronomy**
**Heidelberg University**

Bachelor Thesis in Physics
submitted by

**Luc Marcel Rabitsch**

born in Mannheim (Germany)

**2026**

# Holographic beam shaping for the generation of optical tweezers using a liquid crystal on silicon spatial light modulator

This Bachelor Thesis has been carried out by Luc Marcel Rabitsch at the
Kirchhoff Institute for Physics in Heidelberg
under the supervision of
Prof. Dr. Markus Oberthaler

# Abstract

Liquid crystal spatial light modulators (LCoS SLMs) are a widely used tool for holographic beam shaping and the generation of neutral atom optical traps. This thesis investigates methods for generating and optimizing such optical traps, as well as the suitability of an LCoS SLM for the RuPo experiment, where it is intended for the realization of an Unruh-DeWitt detector. The fundamentals of optical trapping are introduced using a focused Gaussian beam as an example, followed by a description of the operating principle of an LCoS SLM. Methods for generating holograms with and without the Gerchberg-Saxton phase retrieval algorithm are demonstrated. An optical setup is implemented to characterize the different methods of hologram generation and creation of optical tweezers. Using this setup, arrays containing up to 169 individual traps, as well as a variety of other trap geometries, are generated. The trap arrays are successfully optimized to minimize relative intensity deviations between individual tweezers to as low as 1% for a $5 \times 5$ quadratic grid. Finally, the response time of the LCoS SLM is estimated and found to be insufficient for the temporal resolution required by the RuPo experiment. Therefore, the investigated LCoS SLM is found to be suited for the creating of static tweezers arrays but not for the intended application, as in the realization of the Unruh–DeWitt detector.

# Zusammenfassung

Flüssigkristall-Raumlichtmodulatoren (LCoS-SLMs) sind ein weit verbreitetes Mittel zur holografischen Strahlformung und zur Erzeugung optischer Fallen für neutrale Atome. Diese Arbeit untersucht Methoden zur Erzeugung und Optimierung solcher optischer Fallen sowie die Eignung eines LCoS-SLMs für das RuPo-Experiment, in dem dieser zur Realisierung eines Unruh-DeWitt-Detektors vorgesehen ist. Die Grundlagen des optischen Einfangens werden am Beispiel eines fokussierten Gaußstrahls vorgestellt, gefolgt von einer Beschreibung des Funktionsprinzips eines LCoS-SLMs. Anschließend werden Methoden zur Erzeugung von Hologrammen mit und ohne dem Gerchberg-Saxton-Phasenwiederherstellungsalgorithmus untersucht. Ein optischer Aufbau wird realisiert um die verschiedenen Methoden der Hologrammerzeugung anzuwenden und optische Pinzetten-Arrays zu erzeugen. Mit diesem Aufbau werden Arrays mit bis zu 169 einzelnen Fallen sowie eine Vielzahl anderer Fallengeometrien erzeugt. Die Fallen-Arrays werden erfolgreich so optimiert, sodass die relativen Intensitätsabweichungen zwischen den einzelnen Pinzetten bei einem quadratischen $5 \times 5$-Gitter auf lediglich 1% reduziert werden. Schließlich wird die Reaktionszeit des LCoS-SLM geschätzt und als unzureichend für die vom RuPo-Experiment geforderte zeitliche Auflösung befunden. Daher erweist sich das untersuchte LCoS-SLM als geeignet für die Erzeugung statischer Pinzetten-Arrays, jedoch nicht für die vorgesehene Anwendung im RuPo-Experiment zur Realisierung des Unruh–DeWitt-Detektors.

# Contents

**Abstract** **I**

**Zusammenfassung** **II**

**1 Introduction** **1**

**2 Theory** **3**
2.1 Focused Gaussian beam as an optical tweezer . . . . . 3
2.1.1 Optical-potential for RuPo . . . . . 4
2.2 Spatial light modulators . . . . . 5
2.2.1 Liquid crystal on silicon spatial light modulators . . . . . 6
2.3 Holographic beam shaping . . . . . 10
2.3.1 Phase pattern calculation . . . . . 13
2.4 Gerchberg-Saxton algorithm . . . . . 17

**3 Methods** **20**
3.1 Experimental setup . . . . . 20
3.2 Setting-up of the LCoS SLM . . . . . 21
3.3 Implementation of hologram generation algorithms . . . . . 24
3.3.1 Gerchberg-Saxton algorithm . . . . . 24
3.3.2 Weighted Gerchberg-Saxton algorithm . . . . . 28

**4 Results** **31**
4.1 LCoS SLM response time estimation . . . . . 31
4.2 Experimental characterization of a manually generated phase mask . . . . . 32
4.3 Tweezer generation using the Gerchberg-Saxton algorithm . . . . . 33
4.4 Optimization of tweezer arrays using the weighted Gerchberg-Saxton algorithm . . . 37

**5 Discussion** **42**

**6 Conclusion and Outlook** **44**

**References** **46**

**A Wavefront correction** **53**

**B WGS optimization** **55**

# Chapter 1

# Introduction

This thesis was carried out in the cold atom research group *RuPo* [1]. There, many-body atomic quantum systems are studied. One of their goals is to cool rubidium until a Bose-Einstein condensate (BEC) is reached [2]. In this BEC, potassium atom impurities are placed, which could then be used to form what is called a Unruh-DeWitt detector. This detector would then be used to study relativistic quantum field theory, including phenomena like entanglement harvesting from vacuum. The Unruh-DeWitt detector could be realized by trapping a potassium atom impurity in a single well optical potential, which is then dynamically changed to a tilted double well. A thorough analysis of the Unruh-DeWitt detector and entanglement harvesting with regard to potassium impurities in a Rubidium BEC can be looked up in [3].

It was proposed that a liquid crystal on silicon spatial light modulator (LCoS SLM) could be used to construct this optical potential required for the Unruh-DeWitt detector. An LCoS SLM employs special properties of liquid crystals to modulate the phase and/or the polarization of light [4]. This polarization modulating function is commonly used in display technology as liquid-crystal displays (LCD), but the more relevant property for this thesis is the phase modulation possibility. Spatially modulating the phase of a laser beam can be used to shape the optical field into a desired holographic pattern. Because of this technique, liquid crystal spatial light modulators play an important role in creating optical potentials for trapping atoms, also called optical traps [5]. For example, trapping atoms in 2-dimensional [6], 3-dimensional [7], and ultra-precise [8] arrays of optical traps was achieved.

Manipulating atoms with light provides the basis for optical trapping. One force that plays an important part is the dipole force. It's a gradient force that can pull atoms towards regions of higher light intensity depending on the detuning of the light from an atomic transition [9]. This

force can be used to create an optical trap from a single tightly focused laser beam, commonly referred to as an optical tweezer [10].

This thesis investigates methods for manipulating light with a phase-only liquid crystal spatial light modulator (LCoS SLM), commonly referred to as holographic beam shaping, for the generation of optical tweezers. The next chapter introduces the focused Gaussian beam as an optical tweezer and discusses the requirements for the optical potential in the RuPo experiment. It outlines the different approaches for modifying optical potentials, with a focus on LCoS SLMs and their operating principle. The theoretical foundations of holographic beam shaping are subsequently discussed, including analytical methods and the Gerchberg-Saxton algorithm for determining phase patterns required to generate a desired optical field. The experimental implementation is then described, including the experimental setup, the integration of the LCoS SLM, and the hologram generation and optimization methods. The resulting experimental data is presented and evaluated with respect to the SLM response time estimation, the construction, and the optimization of tweezer arrays of different sizes. These results are then summarized and discussed with a conclusion being made about the suitability of an LCoS SLM for the RuPo experiment. Potential improvements and directions for further research, as well as possible alternative approaches, are then discussed.

# Chapter 2

# Theory

## 2.1 Focused Gaussian beam as an optical tweezer

One of the simplest methods to construct an optical tweezer is with a focused Gaussian beam. The dipole force $F_{dp}$ is a gradient force and, for far detuned light, can be written as

$$F_{dp}(\mathbf{x}) \propto -\nabla \frac{I(\mathbf{x})}{\Delta}, \tag{2.1.1}$$

where $I(\mathbf{x})$ is the intensity of the local light field and $\Delta$ is the detuning from an atomic resonance. Depending on the sign of the detuning, the force is either attractive or repulsive. For negative detuning, also referred to as red-detuned, atoms are attracted towards the light field [9].

A focused Gaussian beam, with its longitudinal and radial intensity profiles, is illustrated in fig.2.1. The beam reaches its maximum intensity on the propagation axis at the focal spot. An atom near this position would therefore experience a force pulling it towards the focus. Since the trapping force is proportional to the light intensity gradient, increasing the beam power or reducing the focal spot size, both increase the resulting trap depth. For atoms to be trapped, they need to be cooled such that their thermal energy is sufficiently small compared to the trap depth. In practice, atom temperatures orders of magnitude lower than room temperature, usually in the microkelvin regime or below, are required for them to be trapped [9].

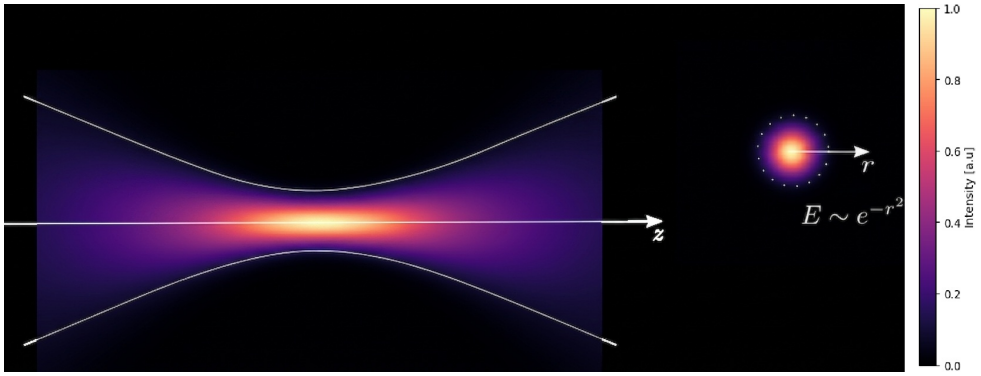



Figure 2.1: Illustration of a focused Gaussian beam with normalized intensity. Side profile on the left and radial profile on the right. Taken from [11], modified.

### 2.1.1 Optical-potential for RuPo

The optical potential requirements needed to realize an Unruh-DeWitt detector in the RuPo experiment place requirements on both the spatial structure and the temporal control of the experimental system [3].

Spatially, $^{41}$K impurity atoms must be localized inside a $^{87}$Rb Bose-Einstein condensate. In the proposed configuration, two impurities are separated by

$$L_{\text{sep}} \approx 1.25\,\mu\text{m}. \tag{2.1.2}$$

At the proposed angular trapping frequency

$$\Omega = 26.3\,\text{krad}\,\text{s}^{-1}. \tag{2.1.3}$$

Where the trapping frequency $\Omega$ characterizes the strength of the confinement and increases with the depth of the optical trap.
Thus, the optical system must produce well-separated traps localizing each impurity to a sub-micrometer region. Similar confinements of $^{41}$K atoms have already been demonstrated in optical tweezers [12] and for $^{39}$K with tweezers generated by an LCoS SLM [13]. However, achieving and characterizing tweezers of comparable dimensions with the present optical setup would require a suitable high-NA objective, which was unavailable. A quantitive investigation of the tweezer dimensions is therefore beyond the scope of this work.

The temporal requirements are a dynamic transformation of the initial potential to a tilted double-

well potential. To perform this potential ramp, the temporal control over the transition must be comparable to the trapping frequency $\Omega$. Converting the angular trapping frequency yields a required potential modulation rate comparable to

$$\nu \approx \frac{\Omega}{2\pi} = 4.2\,\mathrm{kHz}. \tag{2.1.4}$$

Whether an LCoS SLM can provide this temporal resolution will be evaluated in the following chapters.

## 2.2 Spatial light modulators

A single focused Gaussian beam is straightforward to realize; placing a lens or objective in the beam path is sufficient to create an optical dipole trap. In some applications, however, a greater control over the trapping potential is required. Be it for example precise real-time adjustments in the position of the trap or multiple traps that may need to be generated simultaneously, like in the RuPo experiment. The generation of such arbitrary optical potentials can be performed using a spatial light modulator (SLM). In general, an SLM is a device that can control the intensity, phase, or polarization of light with spatial degrees of freedom. Typically, an SLM is illuminated with a coherent light source, such as a laser, and the modulated light is subsequently focused onto the desired trapping region using an objective. Several types of devices are commonly used to achieve spatial control over optical traps, including acousto-optical deflectors (AODs), digital mirror devices (DMDs), and liquid crystal on silicon (LCoS) SLMs [14]. The basic working principle of these three examples is briefly discussed in the following, with a more detailed description of LCoS SLMs, which are used in this thesis.

Acousto-optic deflectors use ultrasound waves propagating through transparent crystals to diffract light. The periodic density fluctuations result in a modulation of the refractive index acting as a diffraction grating, with the beam deflection angle depending on the acoustic frequency. An AOD typically provides beam deflection only along one spatial direction; it's common practice to put two perpendicular to AODs in series to ensure 2D spatial control over the diffracted beam. A major advantage of AODs is their high temporal bandwidth, allowing for rapid changes in trap position. This, however, comes at the cost of a lower spatial degree of freedom.

Digital mirror devices consist of an array of up to millions of microscopic mechanical mirrors arranged like pixels on a monitor. Each individual mirror can be electrically tilted to two set angles. Imaging the beam reflected by only one angular setting turns the two tilt positions into 'on/off' states, resulting in binary amplitude modulation. Similar to the AOD, the fast electric switching

speed of the mirrors provides a high temporal bandwidth, however, with the disadvantage of low diffraction efficiency, partly due to the missing light from 'off'-state mirrors.

Liquid crystal on silicon SLMs operate on a different principle; unlike an AOD or DMD, the light phase is spatially modulated instead of the intensity. An LCoS SLM mainly consists of an electrically controlled birefringent liquid crystal layer, placed on a reflective silicon backplane. By spatially varying the applied voltage, the effective birefringence of the liquid crystals is changed, thus modifying the phase of the reflected light. The large number of independent addressable pixels provides a high spatial bandwidth. The liquid crystals, however, have a long rise time, resulting in, to the AODs and DMDs, comparatively low temporal bandwidth [15].

### 2.2.1 Liquid crystal on silicon spatial light modulators

The main working principle of an LCoS SLM is based on the special properties of the liquid crystal phase. A liquid crystal (LC) is neither a crystal nor an isotropic liquid. They exhibit high fluidity and yet crystal-like properties like birefringence. A material is called birefringent if the refractive index depends on the polarization and propagation direction of light. How this property is used to modulate the phase of light will now be discussed; details on the physics on liquid crystals can be found in [16].

The birefringence stems from the oval, rod-like shape of the LC molecules. A sketch is shown in fig.2.2; the vector $\underline{\mathbf{n}}$ marks the symmetry and optical axis of the LC molecule. Light with an electric field polarization direction perpendicular to the optical axis experiences the ordinary refractive index $n_o$, whereas parallel to $\underline{\mathbf{n}}$polarized light gets refracted by the extraordinary refractive index $n_e$ [4].

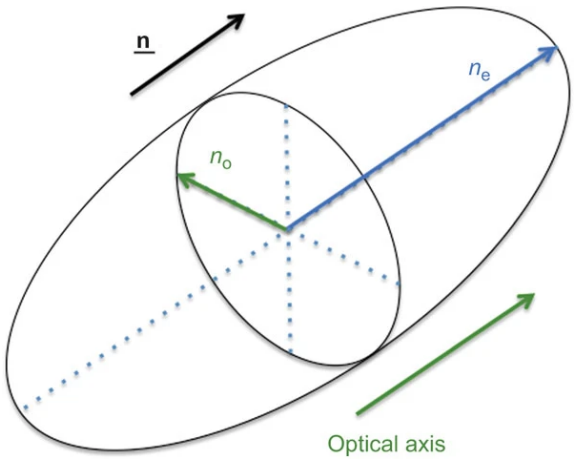



Figure 2.2: Sketch of an oval-shaped liquid crystal molecule with optical indices. **n** marks the symmetry and optical axis of the LC molecule, $n_o$ the ordinary and $n_e$ the extraordinary refractive index. Taken from [4].

By applying an electric field, the LC molecules can be tilted with respect to their initial orientation. This can change the refractive index experienced by light. For instance, starting from an optical axis positioned perpendicular to the light propagation direction, the crystal is turned into a plane parallel to that. For light initially polarized parallel to the optical axis, this tilting motion makes the polarization and optical axis more and more perpendicular. The refractive index changes from purely $n_e$ to an effective refractive index $n_{eff}$ defined in eq.2.2.1

$$n_{eff} = \frac{n_e n_o}{\sqrt{(n_e^2 - n_o^2)\sin^2\alpha + n_0 o^2}} \tag{2.2.1}$$

with $\alpha$ denoting the tilt angle of the LC molecules relative to their initial orientation. This introduces a phase shift in the initially parallel polarized light depending on the twist angle given below.

$$\varphi = 2\pi n_{eff}(\alpha)\frac{d}{\lambda}, \tag{2.2.2}$$

with the thickness of the LC layer $d$ and the wavelength $\lambda$. The 2 stems from the reflective LCoS chip making the light pass through the crystal layer twice. Light which is polarized perpendicular to the optical axis will experience the ordinary refractive index $n_o$ independent of rotation angle. Thus, a liquid crystal SLM can only spatially modulate the phase of light if the polarization is chosen correctly [17].

The structure of the LCoS Chip used in this thesis (Santec SLM-200) is depicted in fig.2.3, with a picture of the real device in fig.2.4 on the bottom. It consists of the discussed liquid crystal

layer placed between two alignment layers, which ensure the desired LC molecule orientation when no voltage is applied [1]. On the other side of the alignment layers are each placed electrodes, one transparent and the other reflective, to apply the electric field to the LC layer. The structure is fabricated on a silicon substrate containing a Complementary Metal-Oxide-Semiconductor (CMOS) circuit, which controls the voltage applied to individual pixel electrodes.

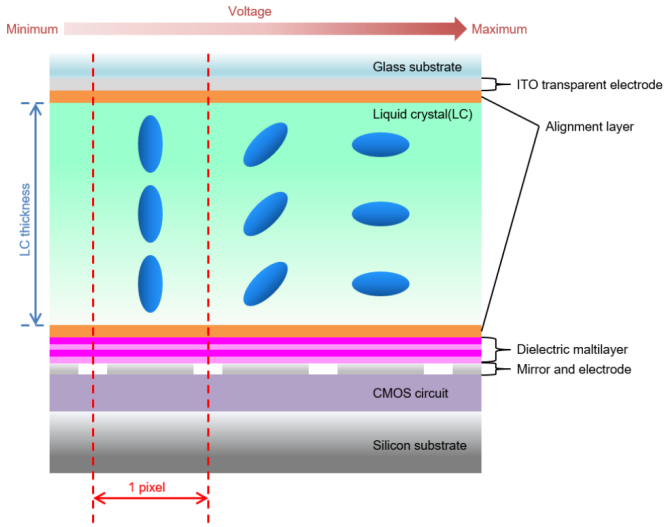



Figure 2.3: Vertical profile of the LCoS SLM *Santec SLM-200* used in this thesis taken from the manual [18]. Consisting of, from top to bottom, a glass layer protecting, a transparent electrode, the liquid crystal layer sandwiched in between two alignment layers, a dielectric multilayer, a mirror electrode, and a silicon substrate containing a CMOS circuit. The chip is divided into pixels, with each voltage being independently addressable, resulting in different tilt angles of the LC molecules.

The whole chip consists of 1920×1200 pixels, which can each be addressed separately with up to 1024 unique voltages, corresponding to phase values in range form 0 to $2\pi$ (fig.2.4). The SLM is operated by loading a phase pattern/mask $\Phi_{SLM}(x, y)$ of either 8-bit (0-255) or 10-bit (0-1023) phase values. Depending on the LCoS device, it can take as long as several hundredths of ms for the liquid crystals to fully respond to the set phase pattern (voltage). Each pixel is the size $7.8 \times 7.8\,\mu$m with a pixel pitch of $8 \times 8\,\mu$m, like sketched in fig.2.4 on the right. The voltage in the space between the pixels cannot be controlled, i.e., the phase. This leads to a strong zeroth diffraction order, which consists of reflected, unmodulated incident light. Unchecked, this zerothorder would be of great annoyance, degrading the target image with a lot of unwanted light. One easy way to get rid of the zeroth-order overlaying with the image is to move the phase-modulated portion away with the blazed grating phase pattern; more on the blazed grating in the next section [19].

[1] Note that the orientation shown in the figure differs from the one used for the above explanation

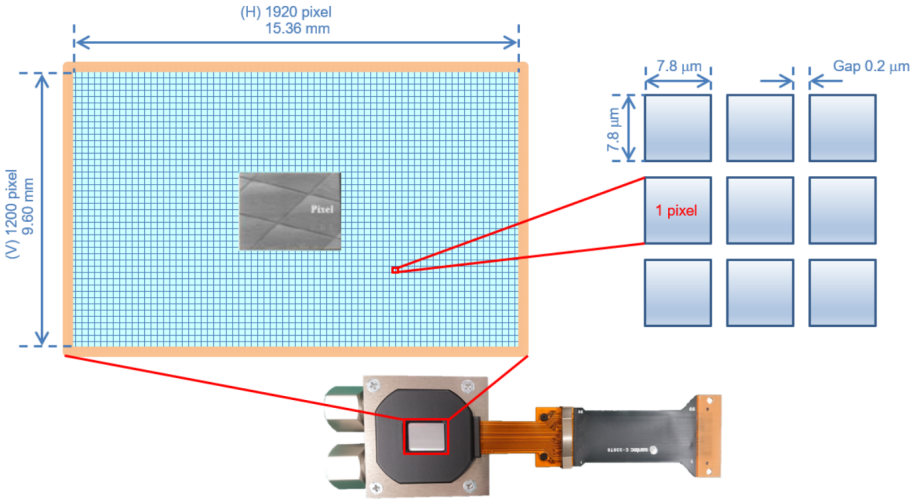



Figure 2.4: Illustration of a top view of the LCoS chip, the pixel pitch and size, and a photograph of the device. The chip consists of an array of 1920×1200 pixels, $15.36 \times 9.6$ mm in size. Each pixel is $7.8 \times 7.8\,\mu$m in size and $8 \times 8\,\mu$m in pitch, resulting in a $0.2\,\mu$m gap in between the pixels. Taken from [18].

### Correction phase patterns

Due to manufacturing limits, LCoS chips are not flat; this varying $d$ in eq.2.2.2 results in a spatially dependent phase response in each pixel. This can degrade the quality of the created optical traps, which is why it is usually compensated by adding a nontrivial correction pattern. A common way is to measure the wavefront of the light coming of the LCOS chip using a Shack-Hartmann sensor when a uniform phase pattern is displayed ($\Phi_{SLM}(x, y) = \Phi_{SLM}$). From this measured wavefront the conjugate is taken and added to the pattern on the SLM, flattening the wavefront [20]. For the used SLM, the manufacturer provided the data from their Shack-Hartmann measurement with their setup and results presented in fig.A.1 of the Appendix. The wavefront profile is plotted in fig.2.5 on the left; this data will now be utilized to calculate a wavelength-dependent correction pattern for this experiment. The measured data was given in optical path difference ($\tau$), which can easily be converted to the phase shift each pixel experiences due to the non-flatness of the LC chip. This phase shift is then compensated with the correction pattern calculated in eq.2.2.3.

$$\Phi_{wf} = \text{mod } 2\pi[2\pi\frac{\tau}{\lambda}] \tag{2.2.3}$$

Using the specific wavelength, the SLM will be illuminated with ($\lambda = 787$ nm). $\Phi_{wf}$ is the so-called wavefront/flatness correction; it is displayed in fig.2.5 on the right. Looking at the wavefront data, you can observe a quadratic phase variation. The manufacturers were able to minimize this by

adding a correction pattern of the same format as calculated, although scaled to a higher wavelength (1064 nm), resulting in a larger ring structure figA.1.

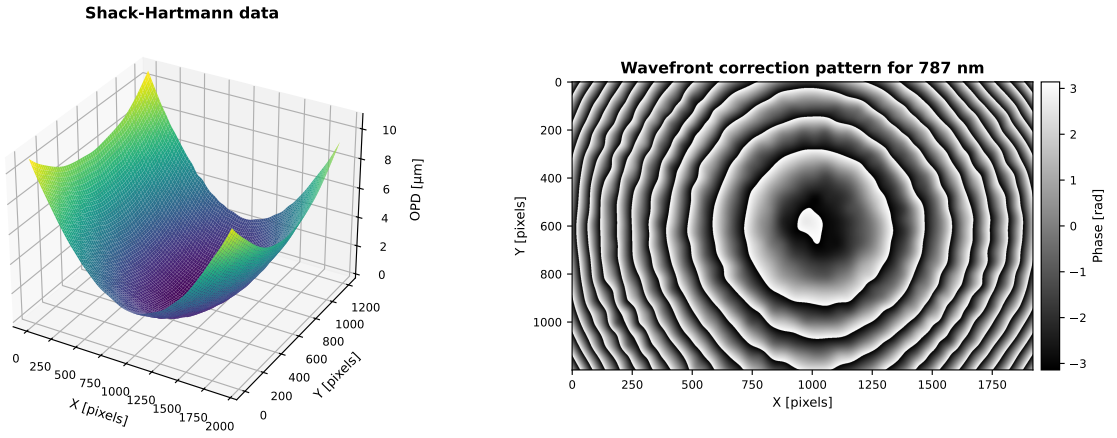



Figure 2.5: Left: Manufacturer provided Shack-Hartmann wavefront sensor data (fig.A.1), optical path difference plotted in $\mu$m. Right: In eq.2.2.3 calculated wavefront/flatness correction pattern for $\lambda = 787$ nm light plotted in gray scale phase values in radians.

Usually another correction is added to counteract aberrations from the other optical elements in the light path, like lenses for instance. This so-called aberration correction can be similarly calculated with the Shack-Hartmann sensor but also with an algorithmic approach. This won't be the subject of this thesis, but for further optimization, it would definitely be of relevance [21, 22].

## 2.3 Holographic beam shaping

As mentioned in the previous section, a LCoS SLM can only spatially modulate the phase of light for a given polarization. Assuming a collimated incident beam with the correct polarization and neglecting its initial phase, the complex field directly after reflection from the SLM can be written as

$$A_{SLM} = \sqrt{I_0(x,y)}\exp[i\Phi_{SLM}(x,y)] \tag{2.3.1}$$

with the initial intensity distribution of the incident beam on the SLM $I_0(x,y)$ and the phase pattern displayed on the SLM $\Phi_{SLM}(x,y)$. Note, on the SLM surface this modulation only affects the phase, not the intensity, as the phase factor drops out when taking the absolute value squared.

$$I_{SLM} = |A_{SLM}|^2 = I_0(x,y). \tag{2.3.2}$$

When the modulated beam is focused by a lens, diffraction and interference transform the spatial phase modulation into an intensity distribution in the focal plane. Mathematically, the complex field in the back focal plane is proportional to the two-dimensional Fourier transformation ($\mathcal{F}$) of the field at the SLM plane resulting in an intensity of [23]

$$I_F(x', y') \propto \left| \mathcal{F} \left[ \sqrt{I_0(x, y)} \exp\left( i\Phi_{SLM}(x, y) \right) . \right] \right|^2 . \tag{2.3.3}$$

The above equation summarizes the principle of holographic beam shaping with an LCoS SLM. The SLM is illuminated with a collimated laser beam with an intensity distribution $I_0(x, y)$. By varying the electrical field applied to the individual pixels, liquid crystals inside the chip twist and spatially modulate the phase of the reflected light, resulting in the phase pattern $\Phi_{SLM}(x, y)$. The reflected beam is focused by a lens ($\propto \mathcal{F}$), and under the Fourier-optics approximation, the intensity distribution $I_F(k_x, k_y)$ is formed in the focal plane.

The remaining task, would be to find phase patterns $\Phi_{SLM}$ that correspond to the desired intensity distribution in the focal plane $I_F(x', y')$. One could think to trivially solve this by inverse Fourier transforming the desired intensity distribution. However, in general an inverse Fourier transformation would yield a complex light field with an arbitrary amplitude distribution on the SLM plane. Since the LCoS SLM is a phase-only modulator, this amplitude cannot be directly realized with the incident laser beam. Determining the suitable phase pattern from a given target intensity distribution is therefore a so called phase-retrieval problem [8].

**Fourier transformation of the Gaussian beam**

A Gaussian beam has the important property that its transverse profile remains Gaussian under a Fourier transformation. To illustrate this transformation property, its radial profile is simplified to one dimension:

$$A_g(x) = A \exp\left[ -\frac{x^2}{2\sigma^2} \right] \tag{2.3.4}$$

with the width $\sigma$ and the amplitude $A$. According to the Fourier-transforming property of a lens discussed above, the complex field in the focal plane is proportional to the Fourier transform, defined

in eq.2.3.5 of the field at the SLM plane. [23]

$$\mathcal{F}\{A_g\} = A_G(k) = \int_{-\infty}^{\infty} A_g(x) \exp[-ikx]\, dx \tag{2.3.5}$$

$$= \int_{-\infty}^{\infty} A \exp\left[-\frac{x^2}{2\sigma^2}\right] \exp[-ikx]\, dx \tag{2.3.6}$$

$$= A \int_{-\infty}^{\infty} \exp\left[-\frac{x^2}{2\sigma^2}\right] [\cos(kx) - i\sin(kx)]\, dx \tag{2.3.7}$$

$$= A \int_{-\infty}^{\infty} \exp\left[-\frac{x^2}{2\sigma^2}\right] \cos(kx)\, dx \tag{2.3.8}$$

$$A_G(k) = \sqrt{2\pi}\sigma A \exp\left[-\frac{k^2\sigma^2}{2}\right] = A_k \exp\left[-\frac{k^2}{2\sigma_k^2}\right] \tag{2.3.9}$$

where the odd integral over a symmetric range in eq.2.3.7 vanishes [2]. The field in the focal plane, has the same radial profile with a transformed amplitude $A_k = \sqrt{2\pi}\sigma A$ and width $\sigma_k = \frac{1}{\sigma}$. Thus, a Gaussian beam focused without any spatially varying phase modulation produces an on-axis Gaussian intensity distribution in the focal plane. To manipulate the position or shape of the resulting tweezer, a spatially varying phase pattern displayed on the LCoS SLM, is required.

For example when multiplying a phase factor $\exp[i\phi(x)]$ to the Gaussian profile with spatial linear increasing phase $\phi(x) = xD$ scaled by some real factor $D$, the Fourier transformation yields:

$$\mathcal{F}\{A'_g\} = A'_G(k) = \int_{-\infty}^{\infty} A \exp\left[-\frac{x^2}{2\sigma^2}\right] \exp[ixD] \exp[-ikx]\, dx \tag{2.3.10}$$

$$= A \int_{-\infty}^{\infty} \exp\left[-\frac{x^2}{2\sigma^2}\right] \exp\left[-i(k-D)x\right]\, dx \tag{2.3.11}$$

$$= A \int_{-\infty}^{\infty} \exp\left[-\frac{x^2}{2\sigma^2}\right] \cos\left[(k-D)x)\right]\, dx \tag{2.3.12}$$

$$A'_G(k) = A_k \exp\left[-\frac{(k-D)^2}{2\sigma_k^2}\right] \tag{2.3.13}$$

again a Gaussian beam $A'_G(k)$, centered at $k = D$. Therefore, multiplying a linear phase factor shifts the Gaussian's spatial frequency.

[2] and a standard Gaussian integral $\int_{-\infty}^{\infty} \exp\left[-ax^2\right] \cos(bx)\, dx = \sqrt{\frac{\pi}{a}} \exp\left[-\frac{b^2}{4a}\right]$ is used

### 2.3.1 Phase pattern calculation

**The blazed grating phase pattern**

Phase patterns that correspond to desired intensity distributions can be calculated analytically or through phase-retrieval algorithms. An easy phase pattern to compute manually is that of the aforementioned blazed grating; this makes use of the above linear phase shift. Physical blazed gratings, as sketched in fig.2.7, are usually made of many periodic ramps that introduce a spatial varying linear phase shift to incident light. The resulting periodic phase modulation causes the light to be diffracted into different diffraction orders, with the diffraction angle depending on the wavelength, grating period, and the angle of incidence. Blazed gratings can, in the right configuration, direct a maximal amount of light into the first diffraction order, making them viable for beam steering and the separation of the zeroth order.

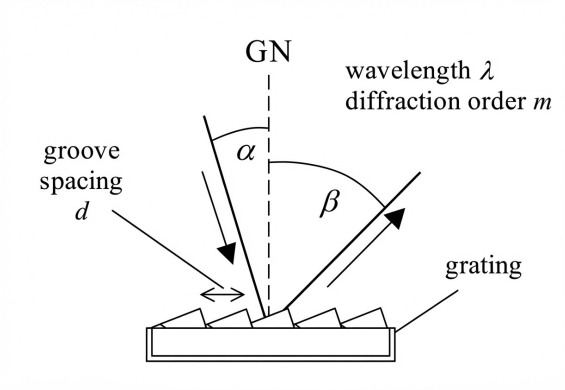



Figure 2.6: Blazed grating sketch with diffraction condition. Incident light, of wavelength $\lambda$, at an angle $\alpha$ to the surface normal GN is diffracted along an angle $\beta$ into a specific order $m$ according to eq.2.3.14. Taken from [24] (up-scaled).

The general diffraction equation for incident light at an angle $\alpha$ to the surface normal of a blazed grating of grating period $d$, with a wavelength $\lambda$, is given by

$$d(\sin\alpha + \sin\beta) = m\lambda. \tag{2.3.14}$$

Where $\beta$ represents the diffraction angle and $m$ the diffraction order [24].

Transferring from a physical blazed grating to a phase pattern for the LCoS SLM is fairly simple. The physical grooves are replaced by a linearly increasing phase ramp wrapped in $2\pi$, resulting in periodic ramps with the same periodicity $d$. To calculate the correct grating period, eq.2.3.14 is simplified. The laser light is assumed to impact the SLM plane perpendicularly ($\alpha = 0$), and $m$ is

set to 1 since only the first diffraction order will be imaged. The expression for grating period $d$ simplifies to

$$d = \frac{\lambda}{\sin \beta} \tag{2.3.15}$$

As an example, computing this for a desired diffraction angle of $\beta = 0.1°$ of light with the wavelength $\lambda = 0.787\,\mu$m, $d = 451\,\mu$m is calculated. Combining this with the pixel pitch of $8\,\mu$m gives the periodicity of the phase ramps, which should be 56 pixels. The phase pattern for this blazed grating is depicted in fig.2.7 with the linear phase ramp on the left and the wrapped phase pattern ready to be displayed on the SLM on the right. The wrapped linear phase ramp can be observed as many vertical fringes.

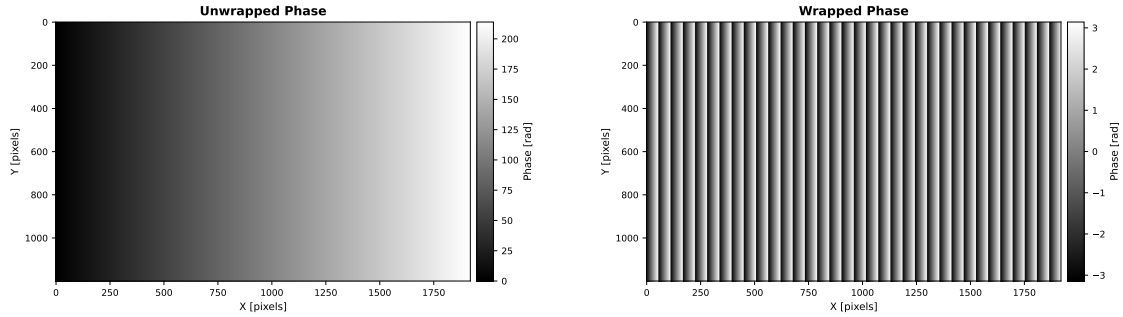



Figure 2.7: Blazed grating phase pattern in units of radians scaled to the LCoS chip. Left: Unwrapped linear phase ramp. Right: Wrapped phase showing vertical fringes with a period of 56 pixels, or $451\,\mu$m.

### The Fresnel lens phase pattern

Another practical phase pattern would be one that imitates a conventional lens, focusing and defocusing the diffracted beam. This would allow for adjustments in the focal spot, i.e., trap position along the beam path ($z$-direction). The quadratic profile of a conventional lens can be imitated by a quadratic phase ramp centered on the LC chip. This phase pattern, also labeled Fresnel lens pattern, is described by the equation below [25].

$$\Phi(\tilde{x}, \tilde{y}) = \text{mod } 2\pi[P\frac{\pi}{\lambda f}(\tilde{x}^2 + \tilde{y}^2)]. \tag{2.3.16}$$

Where $f$ is the focal length of the constructed lens, $\tilde{x}, \tilde{y}$ the pixel coordinates on the SLM display zeroed in the center, and $P$ the pixel pitch relating spatial and pixel coordinates. An exemplary

concave lens phase pattern with a focal length of $f = -50$ mm is depicted in fig.2.8. On the left the unwrapped phase is plotted, which is essentially eq.2.3.16 without the modulus operation, showing a dark spot getting brighter at the edges. The right figure shows the real SLM phase pattern wrapped in $2\pi$. This wrapping results in many centered concentric rings with a decreasing spacing between them. There are also some off-center circular patterns visible, which stem from the finite pixel number leading to aliasing.

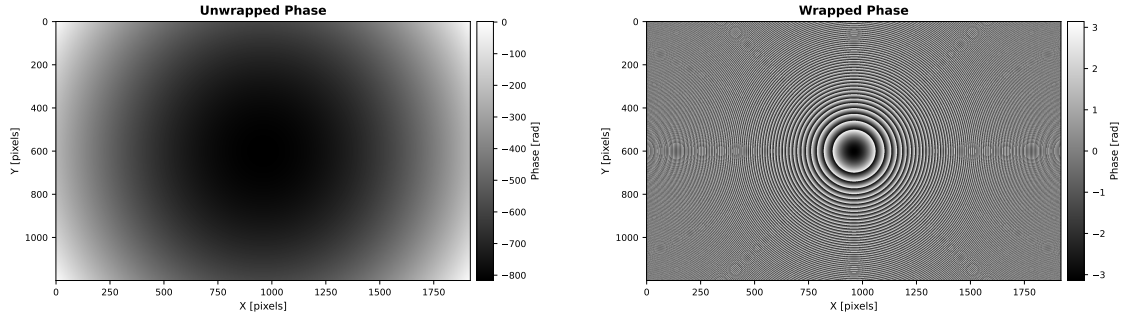



Figure 2.8: Concave Fresnel lens phase patterns with a focal length of $f = -50$ mm. Left: Unwrapped phase, showing increasing phase (brighter pixels) towards the edges of the image. Right: Wrapped phase, resulting in concentric rings with their spacing getting smaller to the edges of the image. Sampling artifacts can be observed as off-centered ring patterns.

### Addition of phase patterns

When combining two or more phase patterns $\phi_j$, a distinction must be made between adding their phases and adding their complex fields. In the first case, the displayed phase is

$$\Phi = \text{mod } 2\pi \left[ \sum_j \phi_j \right]. \tag{2.3.17}$$

with the corresponding phase factor

$$e^{i\Phi} = \prod_j e^{i\phi_j} = e^{i\sum_j \phi_j}. \tag{2.3.18}$$

For linear phase gratings, this means that their induced spatial frequency shifts (eq.2.3.13) are added. For example, for phases $\phi_j(x) = xD_j$, after multiplying to a Gaussian beam and Fourier transforming analogously to eq.2.3.10 yields a Gaussian beam centered at $k = \sum_j Dj$. The result-

ing pattern is therefore producing one displaced beam.

Phase addition is also used to combine different functions of the SLM. For example, a blazed grating $\Phi_{bl}$ for separating the zeroth order, the wavefront correction pattern $\Phi_{wf}$, and the hologram producing the desired trapping potential $\Phi_{trap}$

$$\Phi_{SLM} = \text{mod } 2\pi \left[\Phi_{bl} + \Phi_{wf} + \Phi_{trap}\right]. \tag{2.3.19}$$

On the other hand, adding the complex fields of phase patterns like this

$$\Phi = \arg\left[\sum_j e^{i\phi_j}\right] \tag{2.3.20}$$

where only the phase can be conserved since the SLM provides only phase modulation, which would yield the superposition of the phase patterns due to the linearity of the Fourier transform.
With a mixture of these two addition methods, a square 2 by 2 tweezer array can be constructed. For that, the two blazed gratings shown in fig.2.9 were used. The vertical grating $\phi_x$ on the left diffracts the incoming laser beam horizontally, and the horizontal grating $\phi_y$ on the right diffracts it vertically. Adding their phases ($\Phi = \mathbf{arg}[e^{i(\phi_x+\phi_y)}]$) would diffract the beam diagonally. Using that $-\phi_{x,y}$ mirrors the diffraction direction, 4 phase patterns producing beams in each corner of the square can be calculated, as shown in fig.2.10 on the left. Adding their complex fields yields the final superimposed phase pattern shown on the right of fig.2.10. It looks like a checkerboard pattern with some strange defects in the leftmost columns and upper rows. This phase mask should produce the square tweezer array, which is to be verified experimentally in the results chapter.

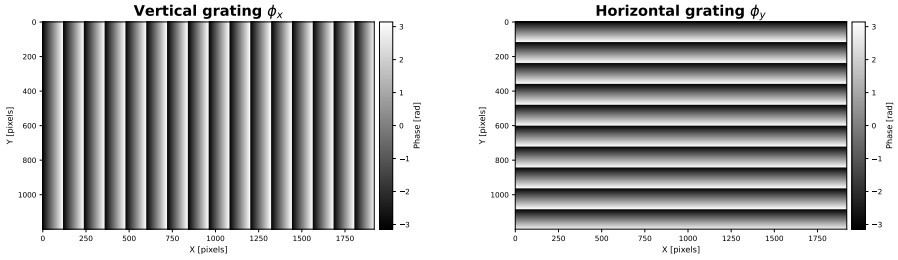



Figure 2.9: Vertical ($\phi_x$) and horizontal ($\phi_y$) blazed grating phase patterns with a grating period of 120 pixels used as a basis to build a 2x2 tweezer array in fig.2.10.

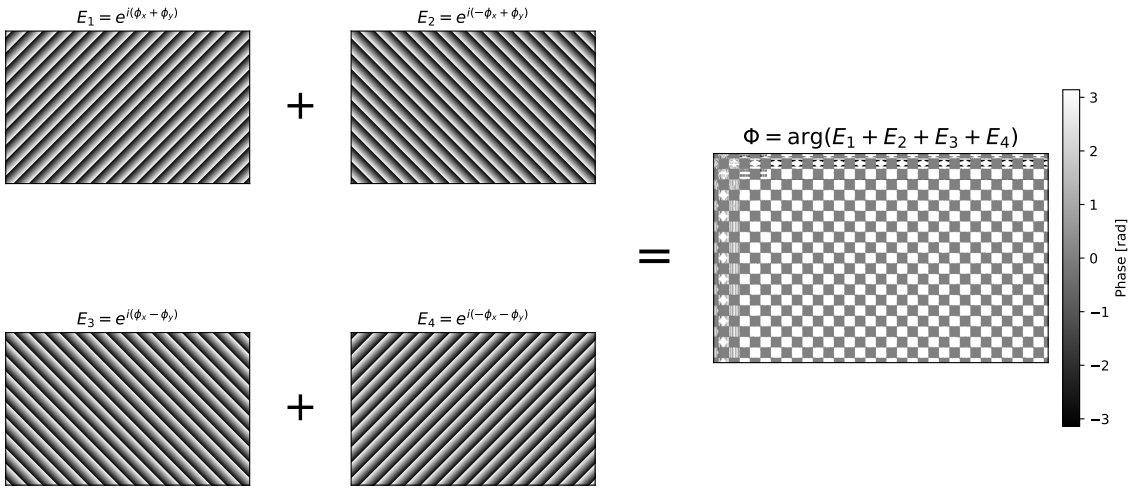



Figure 2.10: Construction of a phase pattern to produce a 2x2 tweezer array when displayed on the SLM. Left part: Both gratings from fig.2.9 $\phi_x$ and $\phi_y$ are combined with modulus addition to make diagonal gratings $E_1$ to $E_4$. Plotted is the polar angle $\mathbf{arg}[E_j]$. Right part: Complex sum of the four diagonal gratings $\Phi = \mathbf{arg}[E_1 + E_2 + E_3 + E_4]$, this yields a checkerboard pattern with defects in the left columns and upper rows.

## 2.4 Gerchberg-Saxton algorithm

The Gerchberg-Saxton (GS) algorithm presents a numerical method to compute the aforementioned phase patterns that generate an arbitrary target intensity distribution. First introduced in 1972 by Ralph Gerchberg and Owen Saxton [26], the algorithm is nowadays widely used for computer-generated holography (CGH) and holographic optical tweezers (HOT) [27] CITE. It employs iterative Fourier transformations to determine the phase mask required to reproduce a given target intensity distribution. The phase-only constraint of the LCOS SLM is incorporated into the algorithm by setting the amplitude of the field in the SLM plane to a constant value in each iteration.

The working principle of the GS algorithm is illustrated in fig.2.11. The left side represents the SLM plane where the phase $\varphi$ can be spatially modulated by the SLM. The right side simulates the lens focal plane where the desired target intensity distributions, like a tweezer array, are formed. The light field in the focal plane of the lens is related to the field in the SLM plane by a Fourier transform, which is numerically implemented using a two dimensional fast Fourier transform (FFT).

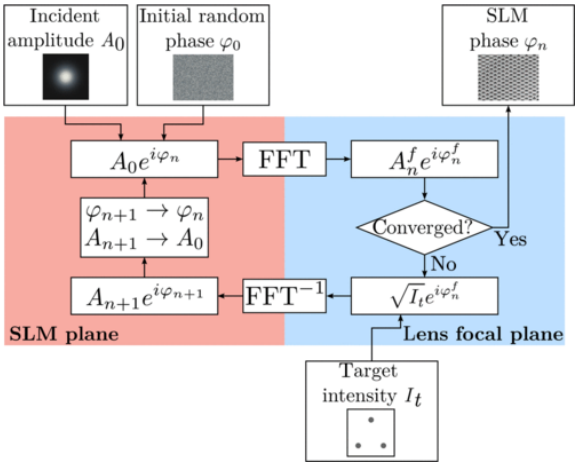



Figure 2.11: Illustration of the Gerchberg-Saxton algorithm. The left side represents the SLM plane, and the right the lens focal plane. Propagation of a light field with an amplitude $A$ and phase $e^{i\varphi}$ from the SLM to the focal plane can be realized with a fast Fourier transform (FFT), simulating the real lens, and vice versa with the inverse $\text{FFT}^{-1}$. Starting on the top left with the light field on the SLM, the field in the lens focal plane is calculated by an FFT. If $(A_n^f)^2$ is not converged to a target intensity $I_t$, an amplitude constraint is applied and back propagation to the SLM plane via inverse FFT is initiated. Here the gained phase information $\varphi_{n+1}$ is combined with the laser amplitude $A_0$, and the next iteration ensues. Taken from [6].

The algorithm has it's starting point on the SLM plane. To the incident amplitude of the laser beam $A_0(x, y)$, where its phase is again neglected, a random phase factor $e^{i\varphi_n(x,y)}$ ($\varphi = \text{rand}[-\pi, \pi]$) is multiplied. The combined light field is propagated to the simulated lens focal plane via the FFT:

$$\text{FFT}[A_0 e^{i\varphi_n}] = A_n^f e^{i\varphi_n^f} \tag{2.4.1}$$

where spatial coordinates $(x, y)$ will be omitted from now on. The resulting amplitude squared $(A_n^f)^2$ is the simulated image, which for now isn't converged. It is set to the desired target intensity distribution $I_t$ while the calculated phase $\varphi_n^f$ is kept and then propagated back to the SLM plane with the inverse fast Fourier transformation ($\text{FFT}^{-1}$).

$$\text{FFT}^{-1}[\sqrt{I_t} e^{i\varphi_n^f}] = A_{n+1} e^{i\varphi_{n+1}}. \tag{2.4.2}$$

In the SLM plane, the phase only constraint is enforced by replacing the calculated amplitude $A_{n+1}$ with the incident laser amplitude $A_0$, while the calculated phase $\varphi_{n+1}$ is retained. The field with which the next iterations is started is therefore $= A_0 e^{i\varphi_{n+1}}$. In that way, the only information of the target intensity distribution is taken from the phase $\varphi_{n+1}$, which is also the only thing the SLM can modulate.

With each iteration $(A_n^f)^2$ will converge more to $I_t$, after the loop is terminated, the calculated phase $\varphi_n$ can be, after adding the previous corrections, displayed on the SLM to form a image resembling the initially given $I_t$ fairly well. Target intensity distribution created from by the Gerchberg-Saxton algorithm, are usually riddled with imperfections like intensity nonuniformities, however. Since the trap intensity is connected to the trap depth, this variation can, depending on the objective, be a problem. When, for example, single-atom trapping is desired, such as in the RuPo experiment, stronger traps may be populated with more than one atom, whereas weaker ones are empty [6].

**Weighted Gerchberg-Saxton algorithm**

These variations can be greatly reduced with the Weighted Gerchberg-Saxton (WGS) algorithm. The WGS algorithm is an optimization method that iteratively adjusts the target intensity distribution based on the resulting diffraction pattern. The intensity distribution (of the diffraction pattern) can be obtained from the simulated diffraction image in the lens focal plane, $(A_n^f)^2$, or through experimental methods. The latter can be obtained by focusing the beam onto camera, but the trap intensities can also be determined directly from the trapped atoms, for example through their densities or via Ramsey interferometry, as demonstrated in the precision tweezer experiment mentioned in the introduction [8].

In this thesis, a variation of the WGS algorithm is implemented to reduce the tweezer-to-tweezer intensity variations in grid tweezer arrays created by the GS algorithm. A camera placed in the lens focal plane is used to capture an image of the array. The intensity of each tweezer is measured, and those with a bellow-average intensity are assigned a higher target intensity, while those with above-average intensity are assigned a lower target intensity and vice versa. Explicitly, the measured intensity for the $n$-th tweezer is denoted $I_n^{meas}$, with the mean over all tweezers given by $\overline{I^{meas}}$. The adjusted target intensity for the $n$-th tweezer is then given as

$$I_{n,i+1}^t = \frac{I_{n,i}^t}{1 - G(1 - I_n^{meas}/\overline{I^{meas}})}, \tag{2.4.3}$$

where $I_{n,i}^t$ is the old target intensity and $I_{n,i+1}^t$ the new. The index $i$ marks the iteration and $G$ an adjustable gain that will be chosen later. A value too low decreases convergence speed, but a value too high leads to overcorrections [6].

# Chapter 3

# Methods

The theoretical principals underlying optical tweezers, holographic beam shaping, phase retrieval and the operation of an LCoS SLM have been established. This chapter describes how these concepts were implemented experimentally using a minimal optical setup.

## 3.1 Experimental setup

The optical setup used to study the LCOS SLM used is depicted in fig.3.1. Although it is made of a minimal amount of optical components, it will suffice for the purpose of this thesis. A titanium sapphire laser tuned to a wavelength of 787 nm is used. The polarization-maintaining fiber outcoupler can be rotated to change the laser polarization axis. The beam is collimated with an achromatic lens to form a Gaussian beam with a width of $2\sigma = 4.7 \pm 1.1$ mm. Two mirrors guide it, with a small angel of incidence needed for good phase modulation [28], to the *Santec SLM-200* LCoS SLM. The displaying of phase patterns is done via the manufacturer-supplied Python API. As a base pattern, a blazed grating is displayed on the SLM, and the first diffraction order is guided with another mirror through the achromatic 1-inch lens F1 ($f = 150$ mm), focused onto the camera (Allied Vision Mako G-223 CMOS). An auto exposure script is used to keep the brightest pixel value in a range between 80 and 90% of the maximum range. Additionally, absorption filters are used to prevent the camera sensor from over saturating.

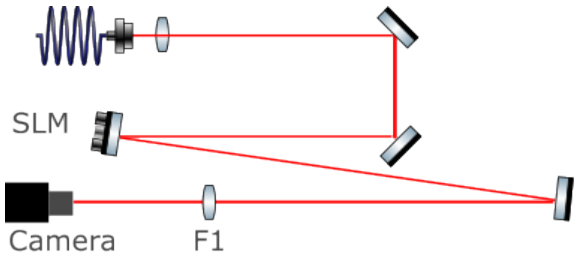



Figure 3.1: Sketch of the used optical setup. The laser light is emitted from the fiber outcoupler on the top left and collimated by the following lens. Two mirrors guide it onto the LCoS SLM on which a blazed grating is displayed. The first diffraction order is then guided with another mirror to the lens F1, where it's focused onto the camera. Models taken from [29].

## 3.2 Setting-up of the LCoS SLM

**Zeroth-order separation**

As a start, just a blazed grating is displayed on the SLM; this separates the phase-modulated light from the unmodulated light. A strong grating with a diffraction angle of 5° at 787 nm is used to reduce the amount of stray light from the zeroth and second diffraction order. The intensity distribution of the focused first diffraction order, captured by the camera, can be seen in fig.3.2. Although the laser intensity was minimized and absorption filters were placed in front of the camera, a non-saturated image of the focal spot could not be taken. This shouldn't be a problem for larger diffraction structures where the intensity is more spread out. For fig.3.2 and all following camera images, the brightness of the pixels is given in arbitrary units of power per area normalized to the brightest pixel labeled as 'Intensity [a.u.]'. For the scope of this thesis the exact values are not of relevance.

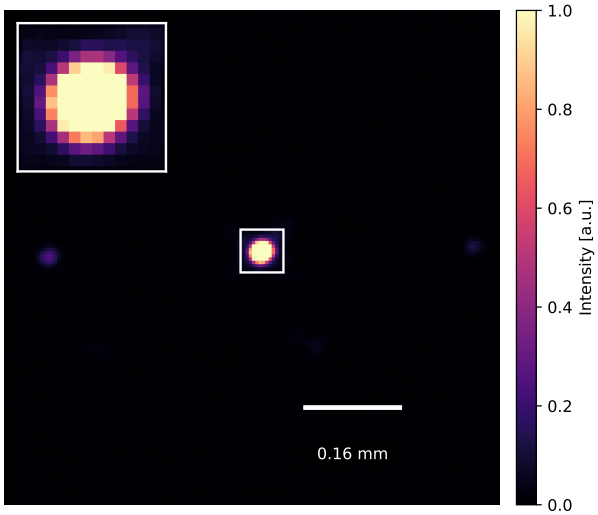



Figure 3.2: Camera image of the focused first diffraction order from a blazed grating displayed on the LCoS SLM. The image shows the oversaturated first order in the center, with one ghost spot on each side.

A clear overexposure maximum with a circular shape is visible. Additionally, two faint spots are to the left and right of the maximum. These so-called ghost spots are secondary diffraction peaks resulting from phase-only modulation of the LCoS SLM [30]).

**Fresnel lens test**

Fresnel lens phase patterns can be used to move the focal spot, i.e., the trap position, in the direction of light propagation. Three different concave Fresnel lens phase patterns are calculated and separately added via modules addition to the blazed grating phase. The in fig.3.3 shown captured camera images show an increase in size compared to the before tightly focused beam (from fig.3.2). Also, substructures like diagonal fringes are observed. Note that no change in the position of either the camera or the lens F1 has been made, meaning the images do not show the focal spot of the beam.

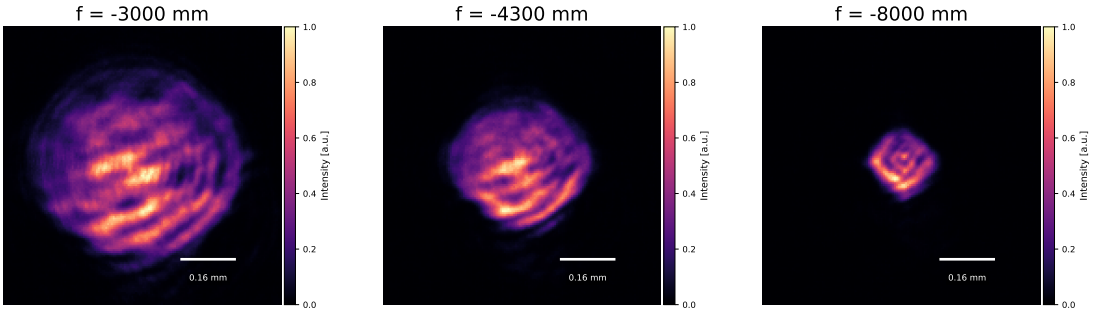



Figure 3.3: Camera image of the laser beam phase modulated by concave Fresnel lens phase patterns of different focal lengths in addition to the blazed grating phase pattern. Images show a beam of varying size that is not focused.

### Wavefront correction

Next, the wavefront correction $\Phi_{wf}$ shown in 2.5 is added on to the grating. The camera image in the previous focal plane of the beam is shown in fig.3.4 on the left. A much larger spot can be seen similar to the Fresnel lens images in fig.3.3. The wavefront correction pattern must act as a concave lens, defocussing the before-collimated beam. The focal length of this, by $\Phi_{wf}$ created, concave lens was measured to be roughly -4200 mm. To account for this defocus, a convex Fresnel lens with a focal length of 4200 mm (phase mask in fig.3.4 middle) is added to the phase patterns. The resulting camera image, displayed in fig.3.4, shows again a focused circle, which is now significantly more oval-shaped than before. With this degradation in image quality in mind, against the literature, the wavefront correction won't be used; a discussion will follow in the next chapter.
For all following phase patterns displayed on the SLM, the (5°) grating pattern will serve as a base pattern to which all other phases will be added with modulus addition.

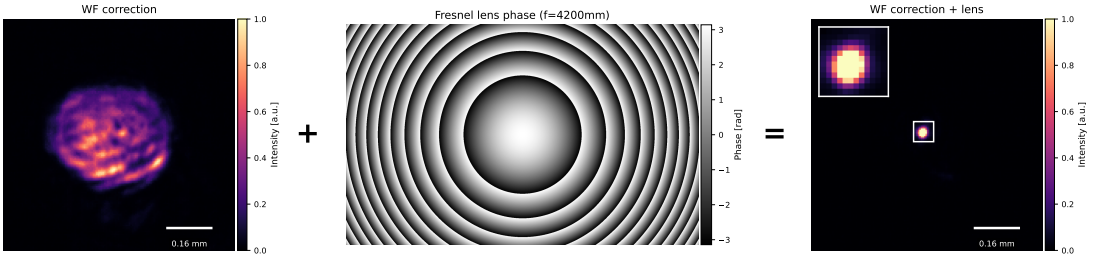


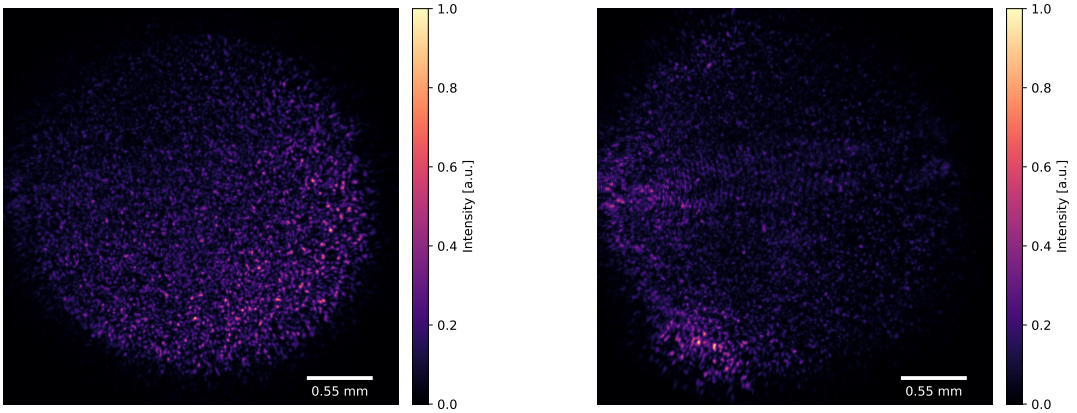

Figure 3.4: Left: Camara image of focused laser beam phase modulated by a blazed grating and the wavefront correction from fig.2.5 showing a larger defocused spot compared to just the grating. Right: Camera image with additionally added convex Fresnel lens ($f = 4200$ mm) shown in the middle to negate defocus. A significantly more oval-shaped focal spot than in fig.3.2 is visible.

## 3.3 Implementation of hologram generation algorithms

### 3.3.1 Gerchberg-Saxton algorithm

When constructing more complex intensity patterns, numerical phase retrieval algorithms can be of great help. The previously discussed Gerchberg-Saxton algorithm is particularly straightforward to implement. It can be written in *Python*, as the numpy library provides the required 2D FFT functionality; the main iteration loop can be written in a few lines of code. The usage of Python is convenient for the present setup, as both the SLM and the camera are also controlled through it. The algorithm takes a suitably scaled target intensity distribution as input and generates the corresponding SLM phase pattern.

The first attempts at generating the desired target intensity distribution directly on the camera failed. At this stage there was no relation between the target image used by the algorithm and the phase-modulated intensity distribution observed on the camera. In particular the spatial scaling between the target image and the camera image. Consequently, target images with inappropriate spatial dimensions were used, of which the resulting phase patterns produced images that could not be properly resolved on the camera. Two of such examples are plotted in fig.3.5.




(a) (b)

Figure 3.5: Camera images of first failed attempts in generating a hologram with the GS algorithm. (a): Attempt of generating a centered Gaussian spot with a too large diameter resulting in a grainy, noise-like pattern. (b): Attempt of generating a 2x2 array of Gaussian tweezers of too large dimensions, clipping outside the focusing lens.

It was established that large target image structures would result in noise like intensity distributions in the focal plane looking at camera pictures. This resulted in strict limits for generating holograms. With the used lens setup, only a center region of the target with a radius of around 100 px could be resolved. Using a larger two-inch lens at F1 would certainly improve this value. Also, a single Gaussian tweezer should be a rather small than large spot in the target image, as a too big of a tweezer leads to a grainy noise-like looking hologram seen in fig.3.5(a). The optimal tweezer size will be discussed more precisely later.

**Generating Gaussian beams of different sizes**

The simplest pattern to generate is one centered Gaussian intensity distribution. The algorithm is run for four different sizes ranging from a width of $\sigma = 0.5$ px to $\sigma = 80$ px, target intensity distribution, camera image and algorithm-generated phase pattern are plotted in fig.3.6. As expected for a Gaussian target, the smallest target, being almost only comprised of one pixel, the algorithm returns a completely uniform phase pattern; every pixel has the same phase value. With increasing size, other almost random-looking substructures are added that reversely decrease in size. From the camera image it's observed that the increase in size is not uniform. The presumed random substructures of different sizes may act like blazed gratings, creating many small diffraction spots

spanning the targeted round shape.

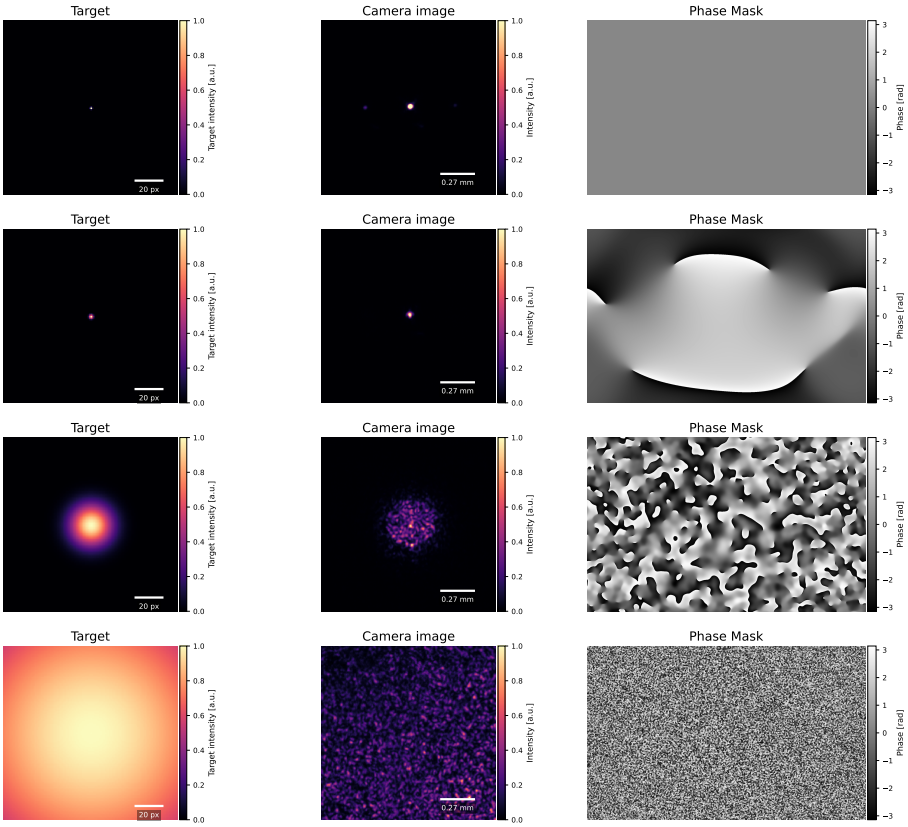



Figure 3.6: Target intensity distribution, camera image and corresponding phase pattern generated by the Gerchberg-Saxton algorithm. The target being a Gaussian beam of different size with a width ($\sigma$) of 0.5, 1, 10 and 80 px starting from the top.

Now, a more in-depth look is taken into the optimal size of the Gaussian spots in the target image. The goal is to achieve a symmetric Gaussian tweezer in the focal spot. The first two rows of pictures in fig.3.7 show single tweezers created from centered Gaussians in the target image with $\sigma_{x,y}$ ranging from 0.5 to 10 px. For 0.5 px and 1 px, the spot is circular shaped but oversaturated. Increasing the size to over 3 px leads to grainy intensity distribution, which is not desired since each of the local maxima would act as its own optical trap. To resolve the 0.5 and 1 px spots better, a $4 \times 4$ grid is created, which spreads out the intensity over the 16 array points. Here the difference becomes apparent. Where the 0.5 px points look almost perfectly round, the 1 px points are very messy, ranging from oval shapes to shadow-like secondary illumination. The $\sigma_{x,y} = 0.5$ px spots will be used for all further pattern generation.

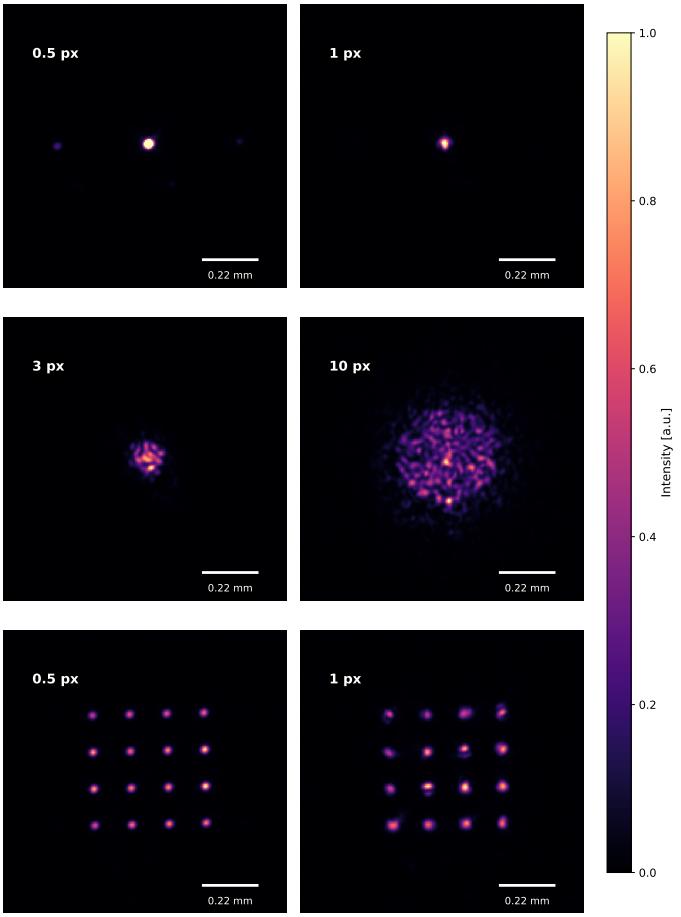



Figure 3.7: Camera picture of Gaussian spots of different sizes ($\sigma_x = \sigma_y$ ranging from 0.5px to 10px) generated with the GS-algorithm. 4x4 Grid on the bottom for non-saturated picture of 0.5 px and 1 px spots.

### Moving the tweezers

The next fundamental task is to move a tweezer in the x- and y-directions. Doing this analytically, one would simply add another blazed grating on the SLM like discussed. Shown in fig.3.8 is the camera image of the shifted spot and the phase pattern created by the GS algorithm. It is visible from the displayed phase patterns that the algorithm converges to the same blazed grating phase pattern.

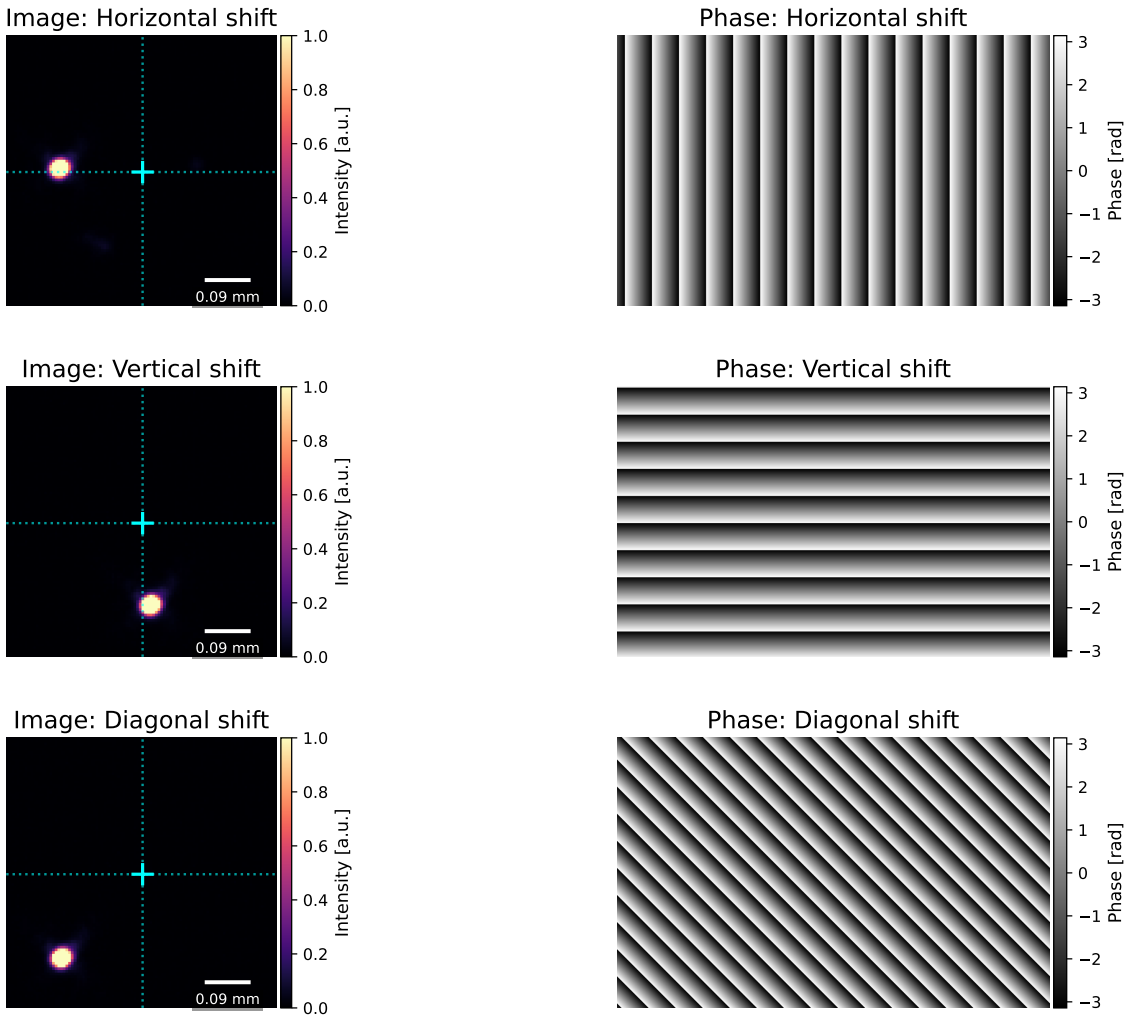



Figure 3.8: Camera image and phase pattern of one Gaussian spot shifted horizontally, vertically, and diagonally with the GS algorithm. Cyan cross marks the unshifted focal position of the base blazed grating. The algorithm converges to blazed gratings.

### 3.3.2 Weighted Gerchberg-Saxton algorithm

#### Modifications made to the target

As mentioned earlier, the intensity distributions created by the GS algorithm usually contain imperfections. One of them can be tweezer-to-tweezer intensity variations, for example, like in the tweezer grid depicted in fig.3.9 on the left. These variations can be reduced by use of the weighted Gerchberg-Saxton algorithm. Starting from the GS-Algorithm array (fig.3.9 left), the tweezer in-

tensity deviations from the mean intensity are calculated. Using eq.2.4.3, a correction is applied to the target image, like illustrated in fig.3.9 on the right. Comparing the grid image and the modified target image, it's observed that weaker spots are increased in their target intensity and brighter ones are decreased. This is done in each iteration of the WGS algorithm, reducing tweezer-to-tweezer intensity fluctuations with each step.

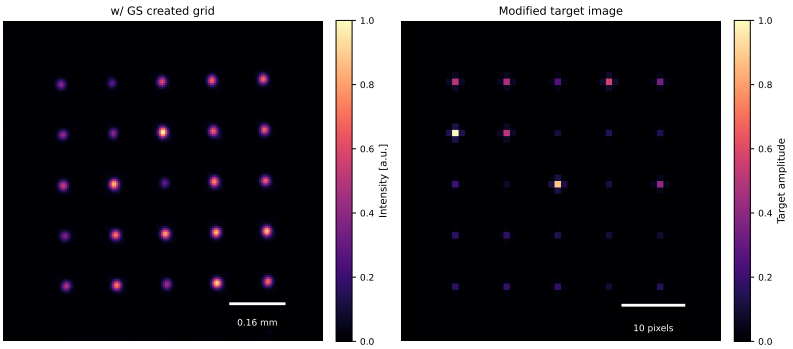



Figure 3.9: Weighted Gerchberg-Saxton algorithm principle. Left: Captured camera image of a 5x5 grid of Gaussian spots created by the GS algorithm with big intensity variations. Right: Modified target image; brighter than average points are reduced in amplitude and vice versa.

### Finding a suitable gain value

Lastly, a proper gain value $G$ to input in eq.2.4.3 needs to be determined to scale the correction applied to the target image. A value that minimizes the intensity variations in few iterations would be optimal. For this, a 6x6 grid is created with the GS algorithm and optimized by the WGS algorithm with different gain values for 20 iterations. In each iteration the relative intensity standard deviation ($\sigma/\mu$) between the tweezers in the grid is calculated and examined. For visualization the relative deviations are plotted in fig.3.10 for the gain values of 0.1, 0.6, and 0.8. In the case of the high gain value, the algorithm makes overcorrections, leading to a big increase in intensity deviations after the initial fast minimum was reached of 0.10. With the low gain value, the intensity deviation decreases slowly, somewhat linearly even, to 0.06, where it increases again. For the optimal gain value of 0.6, a fast decrease to below 0.03 is visible, with it slowly lowering even more to finally the lowest value of 0.02. Because of that and the good convergence behavior with no sudden jumps, this gain value will be used for all the optimization with the WGS algorithm.

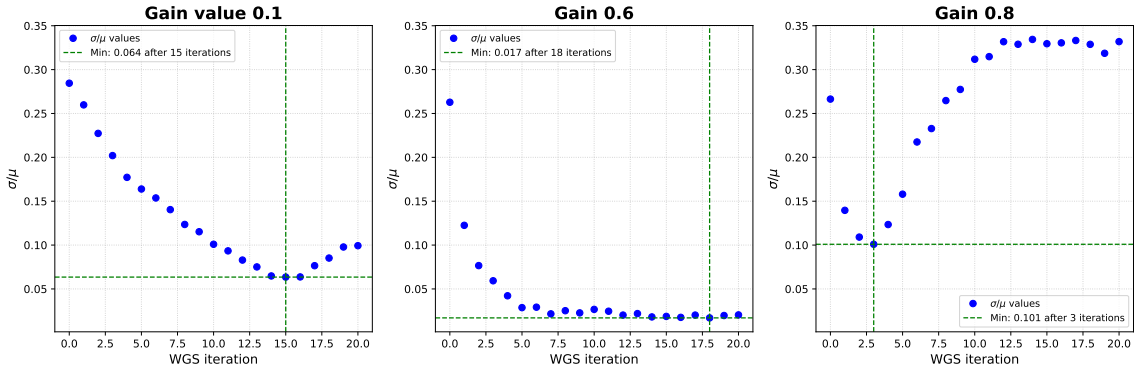



Figure 3.10: The relative tweezer intensity standard deviation ($\sigma/\mu$) plotted against the iterations of the GSW algorithm when optimizing a 6x6 grid target with different gain values ($G$ in eq.2.4.3). A gain value of 0.6 produces the lowest deviation (middle plot). Gain values too high lead to overcorrections (on the right), and values too low (left) do not the lowest deviation.

# Chapter 4

# Results

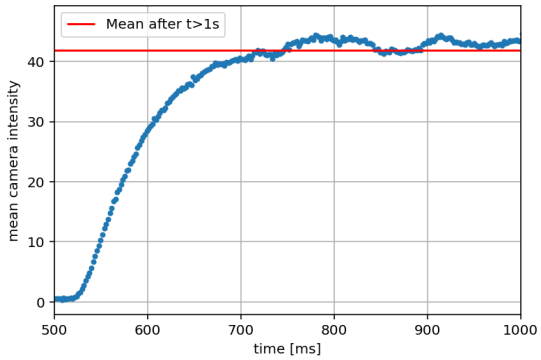
This chapter presents the application of the methods discussed previously. Firstly, it is investigated whether the LCoS SLM can provide the necessary temporal resolution needed for the RuPo experiment. For this purpose its response time is estimated. Next, the manually generated $2 \times 2$ tweezer array phase pattern is displayed on the SLM, and the resulting intensity distribution is compared with that of an equivalent array generated using the GS algorithm. Subsequently, quadratic tweezer arrays with different numbers of tweezers and different inter-tweezer distances are generated, investigating the spatial resolution of the LCoS SLM. The GS section concludes with the creation of several more unconventional tweezer array geometries. Finally, the previously generated quadratic tweezer arrays are optimized in their uniformity using the WGS algorithm, followed by a brief comparison of the convergence behavior of the two algorithms.

## 4.1 LCoS SLM response time estimation

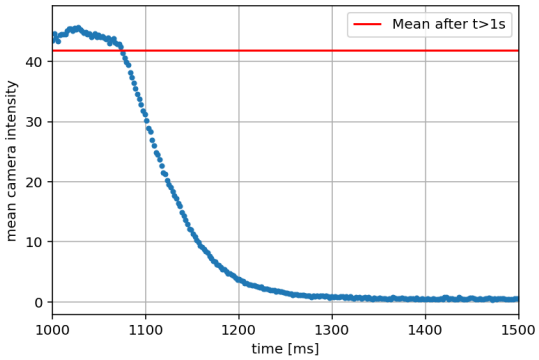
The phase pattern on the SLM is first changed to a uniform factor, making the bright diffraction order form the blazed grating pattern seen in fig.3.2 disappear. Then, while capturing a video with around 1000 fps, the grating is again displayed. The liquid crystals respond to the change in voltage and change their orientation as the camera films the appearing diffraction order increasing in intensity. The disappearance of the diffraction order is recorded as well by switching again to the uniform phase pattern.

From the average light intensity captured by the camera plotted against time in fig.4.1, one can gauge that it takes well over 100 ms for the diffraction order to reach its maximum intensity and then similarly long to drop again. Admittedly, this is not the most sophisticated measuring protocol since electric delays, for example, cannot be resolved. Nevertheless, this sets a lower bound for the

LCoS SLM response time.




(a) Switching on the blazed grating leads to a saturating increase in average captured camera intensity.




(b) Switching on the blazed grating leads to a saturating decrease in average captured camera intensity.

Figure 4.1: Measuring of the response time of the *Santec SLM-200* by switching a blazed grating on and off. The average camera pixel intensity value is plotted against the time with a resolution of around 1000 Hz. The appearing (a) and disappearing (b) of the diffraction spot captured in fig.3.2 are resolved in time by the graphs.

## 4.2 Experimental characterization of a manually generated phase mask

As stated in the theory chapter, an array of tweezers can be created from the addition of only 2 blazed gratings. The $2 \times 2$ array phase pattern created in fig.2.10 is now displayed on the SLM. The resulting camera image is plotted in fig.4.2, where the 4 array spots are clearly visible. In addition to that, many more unwanted ghost spots can be seen.

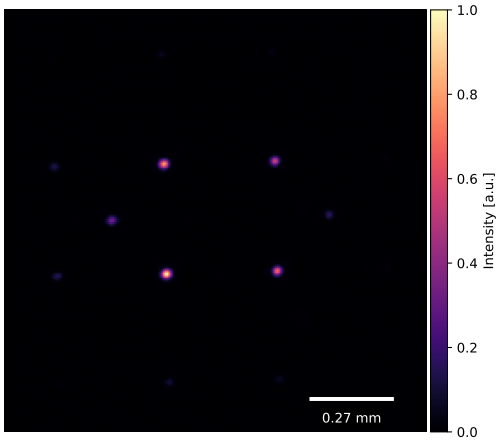



Figure 4.2: Camera image of focused laser beam phase modulated by the 2x2 array phase pattern in fig.2.10. The desired 4 diffraction spots are visible with several unwanted ghost spots.

## 4.3 Tweezer generation using the Gerchberg-Saxton algorithm

**Tweezer arrays**

Like seen in fig.3.7 above, tweezer arrays can be constructed using the GS algorithm. First, the $2 \times 2$ grid created in fig.2.10 and displayed in fig.4.2 is recreated with the algorithm. The camera image and phase mask can be seen in fig.4.3 below. The image shows the 4 tweezers, and now only 4 without any ghost spots visible. In the phase pattern picture definite similarities are visible. It's in principle the same scaled checkerboard pattern but additionally contains diagonal smudges. These smudges are probably optimized by the algorithm to minimize higher diffraction orders that would otherwise create the unwanted ghost spots.

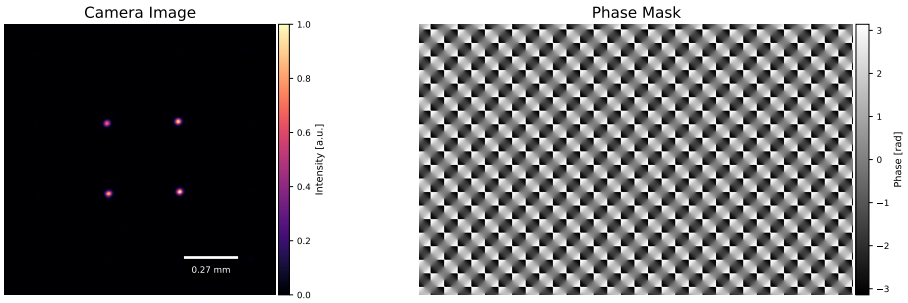



Figure 4.3: Camera image of algorithm generated $2 \times 2$ grid with phase mask (manually generated grid in fig.4.2). No ghost spots are visible.

Some more tweezer arrays are plotted in fig.4.4 with up to 100 single tweezers. The round shape of each tweezer is visible for each size, but for the larger arrays on the edges there are some deformities. Here the circular shapes turn elliptical and are radially oriented (pointing to the center). These are aberrations that could be caused by the optical setup, in this case mostly the lens F1. Using the setup-specific aberration correction addressed in sec.2.2.1, these could be minimized. Another issue is the varying intensities of the different tweezers. For the 5x5 grid a relative deviation, where the standard deviation of the tweezer intensities is divided by the mean intensity, is calculated as 29% and for the 10x10 grid even as high as 41%. These deviations are not purely to blame on the GS algorithm, as the upper left corner receives significantly less light than other areas. This was tried to solve on multiple occasions but in the end could only be minimized.

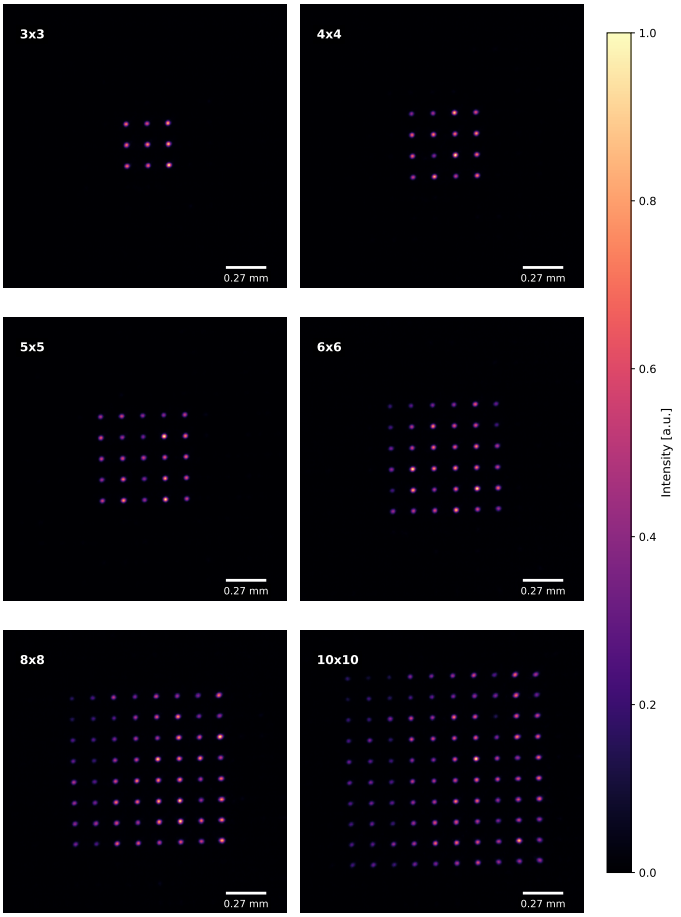



Figure 4.4: Camera images of different point arrays, phase mask generated by the GS algorithm. The top left label marks the size of the array. Aberrations in the outer tweezers and intensity nonuniformities are visible for larger array sizes.

### Minimal separation of tweezers

For the realization of the Unruh-DeWitt detectors in the RuPo experiment, the potassium atoms should optimally be separated by 1.25 $\mu$m. For that reason, it is investigated how close the tweezers can be moved together without compromising their quality. This is tested with a $4 \times 4$ array of Gaussian targets separated by varying distances displayed in fig.4.5. Arrays with separations between 1 and 8 pixels in the target image are looked at. The picture in the top left corner shows a tweezer array separated by only one pixel; here no singular spots can be distinguished, only one big deformed dot is visible. For the two- and three-pixel-separated array pictures, every array point is

visible, but the quality is impacted by the small separation with many non-round-shaped tweezers. This improves with larger separations until, for the 8-pixel array, every tweezer looks to be round. The average tweezer separation for the 3-pixel array is calculated to be $46\,\mu$m with a standard deviation $\sigma = 3\,\mu$m, which is almost two orders of magnitude higher than the desired separation in the RuPo experiment and compromises tweezer quality.

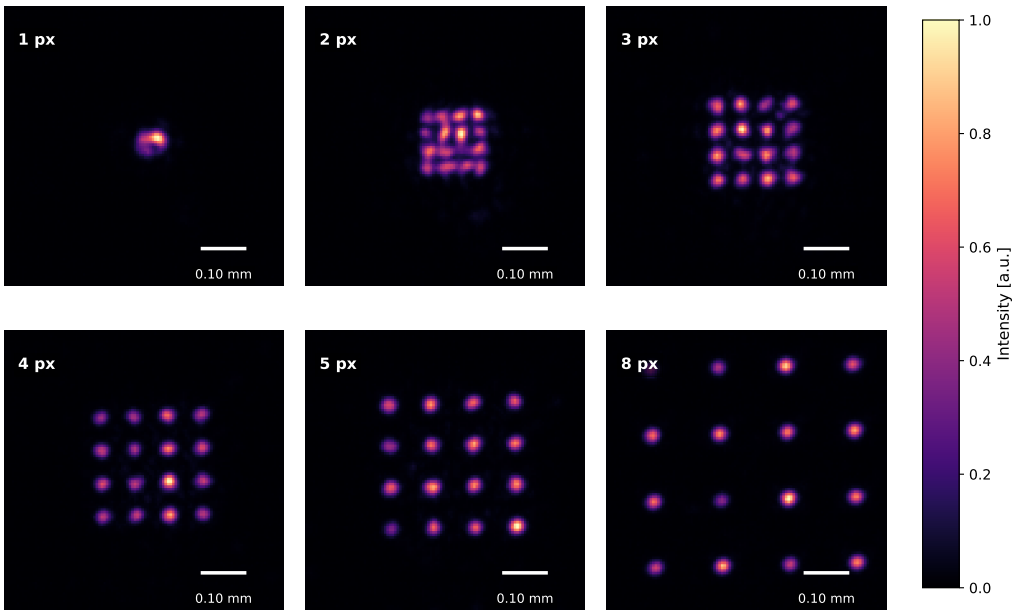



Figure 4.5: Camera image of a $4\times4$ Gaussian tweezer array created by the GS algorithm with varying spacing in the target image ranging from one to eight pixels. For a spacing of less than 8 pixels, the tweezer quality degrades significantly; in the 1 px image, no single spots are distinguishable.

### Arbitrary intensity patterns

To end this section on the GS algorithm, out of curiosity, a range of different target shapes are imputed in the algorithm. Targets, camera pictures and phase patterns are plotted in fig.4.6. The structures given in the target image were recreated by the algorithm, with the before described flaws as the intensity drops towards the top left corner, and aberrations are visible. The bottom camera picture shows that not only arrays of Gaussian spots can be realized, but also hand-drawn images.

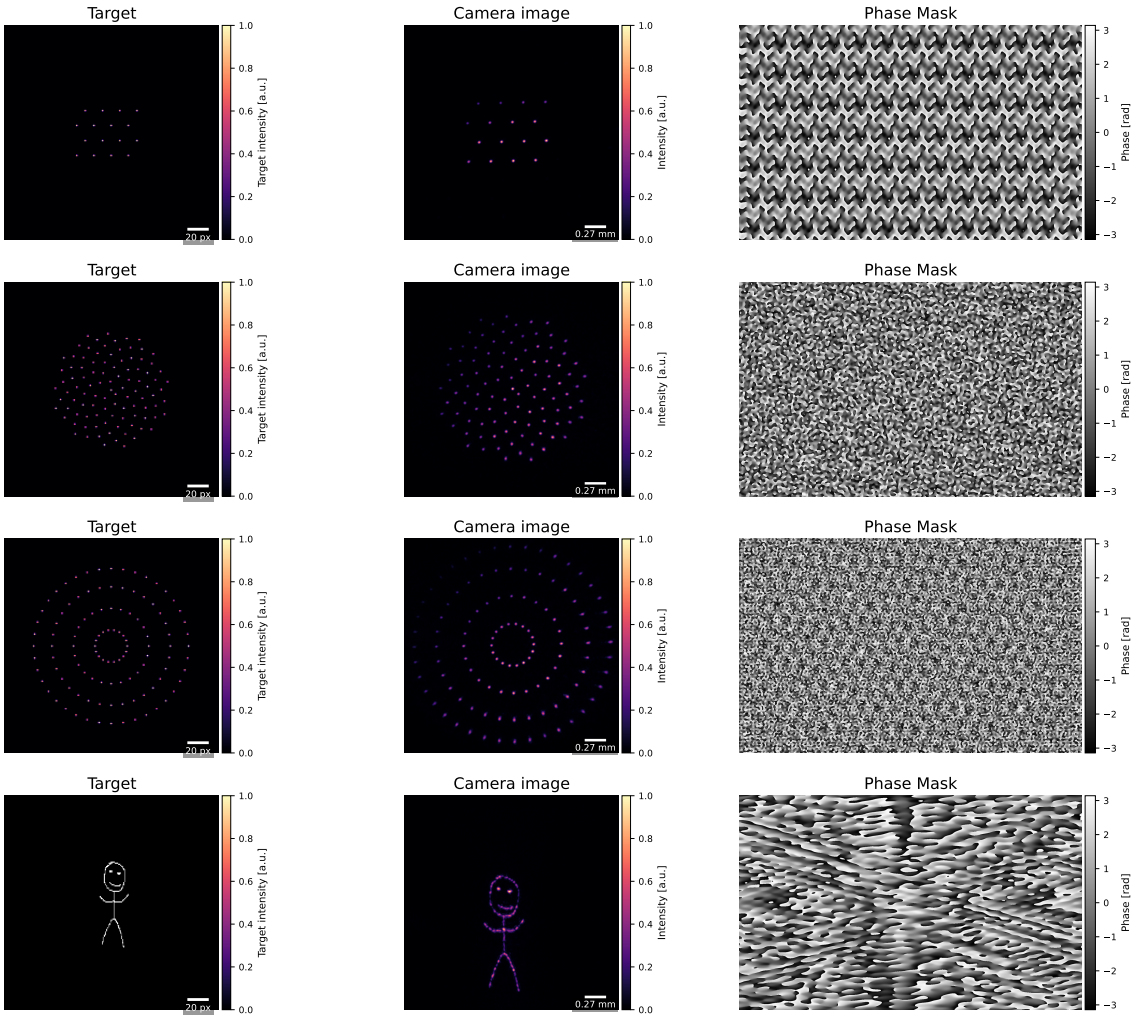



Figure 4.6: Plot of different target images with corresponding camera images and phase patterns created by the GS algorithm. Going from top to bottom, a hexagonal lattice, a Fermat (sunflower) spiral, concentric rings, and a hand-drawn stick figure target are plotted.

## 4.4 Optimization of tweezer arrays using the weighted Gerchberg-Saxton algorithm

As seen, with the help of the GS algorithm, a range of different intensity distributions can be constructed quite easily. However, the result is usually riddled with imperfections like intensity nonuniformities. Looking at the 5 by 5 grid in fig.4.7a) created using the GS algorithm, we see a

broad intensity distribution in each tweezer. A relative error of 29% to be exact, the histogram in fig.4.7b) also shows the extent of the deviations from the average. This metric is optimized with the discussed WGS algorithm, where the target intensity pattern is changed in each iteration correspondingly to the camera image.

The optimized image is plotted in fig.4.7c); visually, the homogeneity in intensity is quite protruding. Every tweezer seems to have the same intensity, contrary to the GS picture in a). Looking at the histogram with the exact data in fig.4.7d), the observations are confirmed. The relative standard deviation decreased from 29% to as little as 1%, and the 8-bit intensity values only span from around 206 to 214, in contrast to 80 to 220.

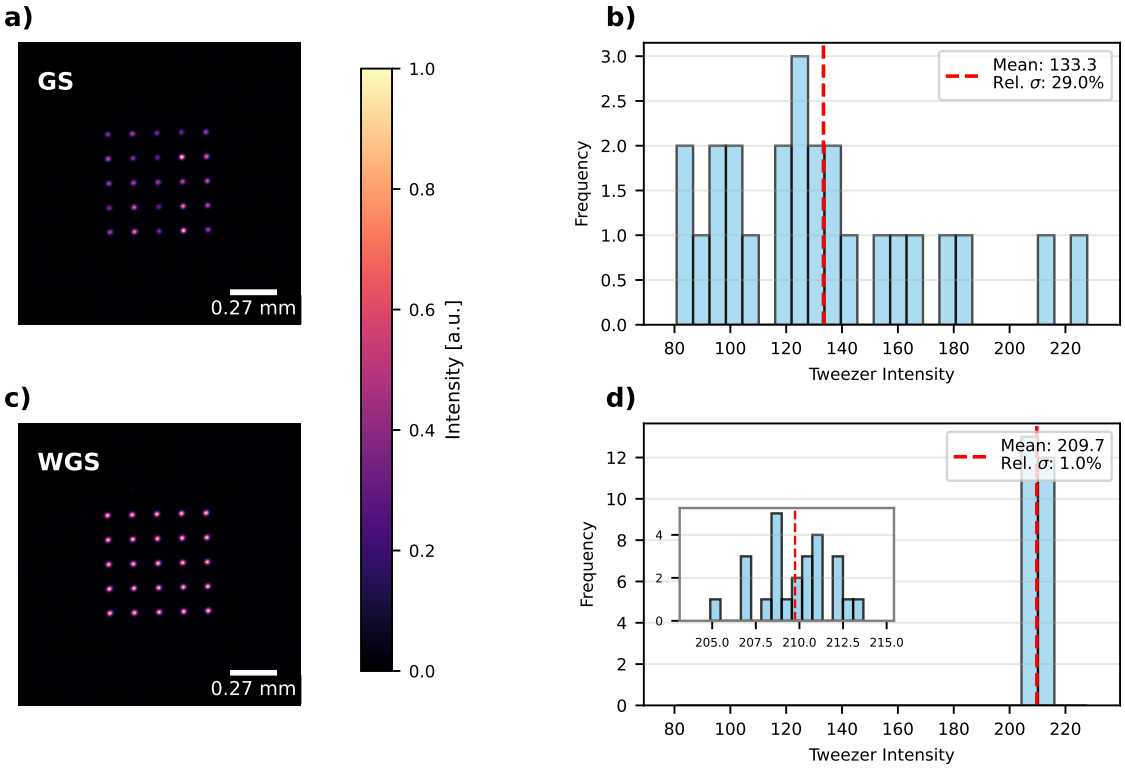



Figure 4.7: Comparison of the GS-algorithm-created tweezer array with that optimized by the WGS-algorithm. a): Camera image of 5x5 tweezer array created with the GS algorithm with the corresponding histogram of tweezer intensities in b). c), d): analogous with the WGS algorithm. From GS to WGS, a drastic decrease in tweezer to tweezer intensity variations is visible and measurable as the relative standard deviation ($\sigma/\mu$) decreases from 29% to 1%.

Furthermore, all the GS-created arrays from fig.4.4 are WGS-optimized and plotted in fig.4.8.

Throughout all array sizes, the intensity variations look to be improved significantly by the optimization process. A detailed plot for each grid similar to fig.4.7 can be found in the appendix fig.B.1-B.5. The deformities of the outermost tweezers due to aberrations have not changed and present a problem that would still need fixing.

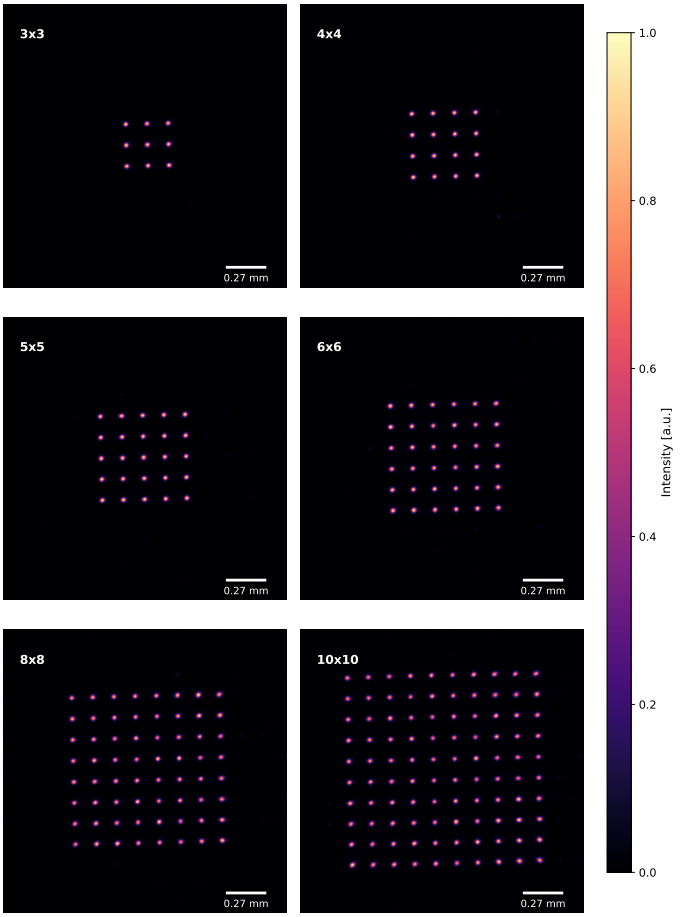



Figure 4.8: Camera images of the same point arrays as fig.4.4 ranging from 3x3 to 10x10 optimized with the WGS algorithm. Histogram comparison alike fig.4.7 in the appendix fig.B.1-B.5.

To test out the limits of the optimization algorithm, a larger 13x13 tweezer array is constructed and optimized. The results shown in fig.4.9 paint a different picture than those for the 5x5 array. To begin with, in the GS image the visible nonuniformities have increased drastically, and many more ghost spots are visible. The WGS-optimized grid is a definite improvement, as every grid tweezer is easily visible, but also there are many more ghost spots. In addition to that, the data only shows a decrease in the relative deviations from 48% to 19%, which is only around a 2-fold

decrease compared to the 30-fold decrease for the 5x5 grid.

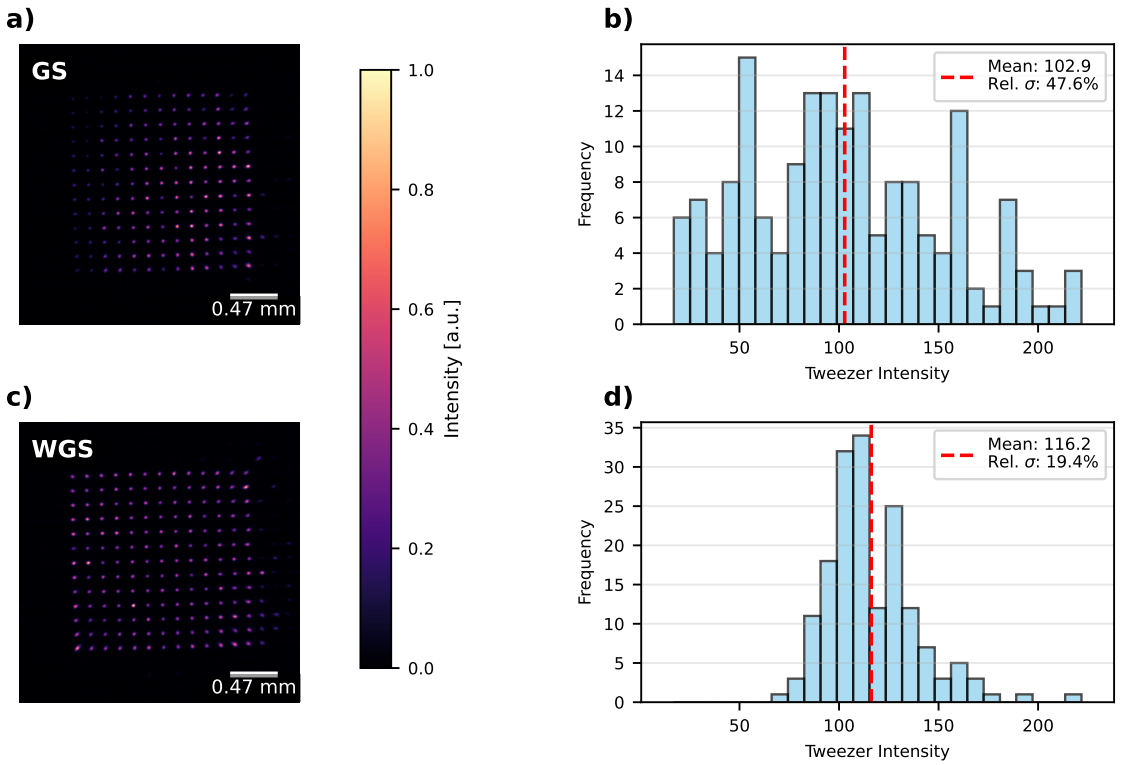



Figure 4.9: Comparison of the GS-algorithm-created tweezer array with that optimized by the WGS-algorithm. a): Camera image of 13x13 tweezer array created with the GS algorithm with the corresponding histogram of tweezer intensities in b). c), d): analogous with the WGS algorithm. From GS to WGS, a decrease in tweezer to tweezer intensity variations is visible and measurable as the relative standard deviation ($\sigma/\mu$) decreases from 48% to 19%. This decrease is much smaller compared to that of the 5x5 array; also, after the optimization, many ghost spots appear on the image.

### Convergence behavior of the algorithms

The relative intensity deviation was recorded in each iteration of the GS- and WGS-algorithm, providing a picture of the convergence speed. A side-by-side plot for the 5x5 (from fig.4.7) and 13x13 (from fig.4.9) arrays is shown below in fig.4.10. One clearly notices the much faster convergence in the GS algorithm for the smaller array, where around 5 iterations lead to a minimal deviation, with it increasing after that. Whereas for the 13x13 array convergence might be reached after 15 iterations, but from the look of the graph more iterations could very well lead to further improvement. With

the WGS algorithm, the larger array converges around 5 iterations faster but to a much higher value.

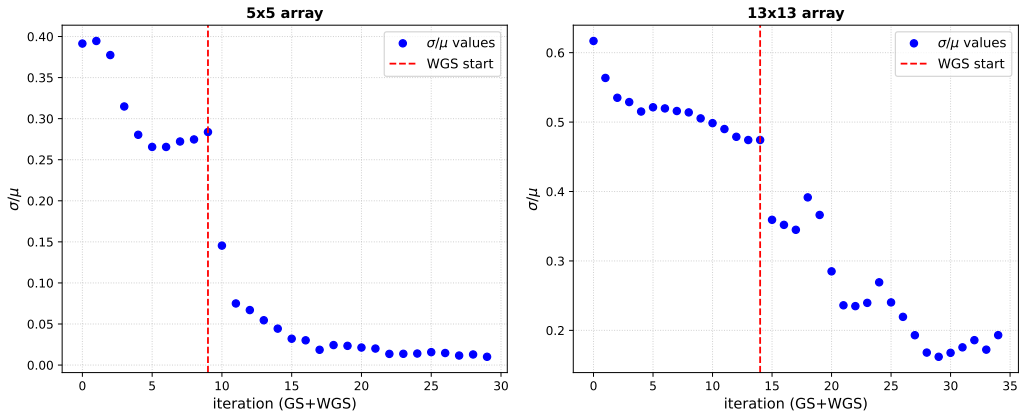



Figure 4.10: Plot of the relative intensity deviation ($\sigma/\mu$) against the iteration of the GS- and WGS-algorithm in the creation of two array targets. The red vertical line marks the switch from GS to WGS. Left: Corresponding data for the 5x5 array from fig.4.7; Right: Corresponding data for the 13x13 array from fig.4.9. The smaller array has a much faster convergence speed for both algorithms and reaches lower deviations.

# Chapter 5

# Discussion

In this thesis, holographic beam shaping with a liquid crystal spatial light modulator was demonstrated. A simple setup was built to apply before explored methods of generating holograms. Beam steering was performed with calculated blazed grating phase patterns. By that method the zeroth-order was separated, and a $2 \times 2$ tweezer array phase pattern was calculated through a combination of two grating patterns. Fresnel lens phase patterns were used to defocus the beam, moving the tweezer along the propagation axis.

It was proceeded with an implementation of the Gerchberg-Saxton phase retrieval algorithm to create holograms from a target intensity distribution. It was found that when using the GS algorithm, smaller target tweezer sizes produce as in rounder and smoother tweezers in the focal plane. Within the tested parameter range, increasing the tweezer resulted in increasingly structured or 'grainy' intensity distributions, compromising its trapping application. When a $2 \times 2$ tweezer grid was constructed by composing 2 blazed gratings, the observed grid was of plagued with ghost spots, not however that of the GS algorithm when prompted with the same task. The resulting phase patterns look quite alike, but the algorithm-created phase pattern shows slight modifications, probably improving diffraction into the 4 desired tweezer spots. This demonstrates the advantages of the GS algorithm for generating more complex intensity distributions, where direct analytical construction becomes increasingly difficult.

More tweezer arrays with a range of geometries were constructed using the GS algorithm. These exhibited large tweezer-to-tweezer intensity fluctuations that were partly due to the optical setup but also a known problem of the algorithm. As a next step, the created tweezer arrays were optimized using the weighted Gercberg-Saxton algorithm. For the small $5 \times 5$ tweezer grid, the intensity variations were reduced from 29% relative error to as low as 1% relative error. This was not reproducible

for larger grid arrays; the largest created $13 \times 13$ array could be reduced in intensity variations from 48% to 19%. This could be attributed to more competing constraints in the algorithm, a perhaps array-dependent gain value and also a lower convergence speed.

One factor impacting the quality of the generated tweezer arrays was aberrations, likely originating from the optical setup, as these became noticeable only when generating larger structures reaching the edges of the focusing lens. A, to the optical setup tailored, aberration correction phase pattern could be used to reduce these.

In regard to the proposed use of an LCoS SLM in the RuPo experiment and the therefore required dynamic potential ramp, the dynamic capabilities of the SLM were tested. The lower bound of the response time was determined to be in the low hundredths of milliseconds, which is in agreement with the 200 ms given in the instruction manual, stated to be dependent on the displayed phase pattern. Such a slow temporal bandwidth is insufficient for the required dynamic potential ramp. Additionally, the necessary spatial dimensions of the tweezers, could not be directly replicated. Only an observation was made that with decreasing tweezer-to-tweezer distance, the quality, as in shape uniformity, worsened significantly.

It was also found that applying the wavefront correction introduces a Fresnel lens-like defocussing effect, which was then compensated with a focusing Fresnel lens phase pattern. This phase pattern, made for the improving of tweezer shape and intensity, was found to be worsening overall diffraction quality and was therefore discarded. A pure correction of the SLM's intrinsic aberrations would not be expected to introduce an uncompensated defocus in the present setup. This suggests that the applied correction pattern does not correspond to the correct phase pattern. Even more interesting is that the measured wavefront from the manufacturer shows a quadratic bowl-like shape which should, like examined when the Fresnel lens phase pattern was discussed, not coincide with a collimated beam. But when there is no phase pattern and when just the blazed grating for separation of the zeroth-order is displayed, no visible defocus or such could be observed. Only when the presumed correction pattern was added did the collimated beam turn defocussing. Since the correction pattern was not provided for the used wavelength, a calculation error cannot be ruled out. Although the wavefront correction sign was flipped with no success (fig.A.2), the scale of the correction pattern, as in the number of concentric rings, matches the decreased wavelength. Despite that, the created holograms did not show any defects that could be linked to the unused wavefront correction.

# Chapter 6

# Conclusion and Outlook

With the presented optical setup, holographic beam shaping could be performed. Analytically calculated phase patterns such as blazed gratings and Fresnel lens phase patterns were being utilized for beam steering in the radial and longitudinal directions. With the implemented Gerchberg-Saxton algorithm, a range of tweezer array geometries could be created and imaged on a camera. For smaller-scale grid arrays, the optimization of tweezer-to-tweezer intensity variations with the weighted Gerchberg-Saxton algorithm was of great success. Adjustments in the optimization scheme could be implemented to improve the intensity variations for larger arrays. For example, an array-specific optimized gain value or completing more iterations of the algorithm. Predominantly with larger tweezer arrays, intensity defects became an issue. One of them was unwanted diffraction orders called ghost spots, which can be reduced by software, characterizing the SLM beforehand and applying a correction to the displayed phase patterns [30]. Other problems were the occurrence of aberrations from the optical setup, namely the focusing lens. These can be corrected by measuring the wavefront and adding a corresponding correction phase pattern. The correction pattern calculated from the manufacturer-provided wavefront data was found to introduce an unexpected defocusing effect and was therefore not used for the generated holograms. Implications of this missing wavefront correction pattern could not conclusively be observed.

For trapping atoms with the constructed tweezer arrays, a high NA objective would additionally be required, focusing the tweezers to create the strong enough intensity gradients for trapping. Then, a new telescope after the SLM would be required for the beam to match the size of the objective's back aperture [31]. Future work could also investigate the effects of different incident beam diameters on the SLM, which was not tested here. This would then require ano ther telescope in front of the SLM.

One goal of this thesis was figuring out if the used LCoS SLM was suitable for use in the RuPo

experiment. The desired realization of the Unruh-DeWitt detector would require a dynamic transition from a single well to a tilted double well optical trap. For this dynamic potential ramp, a high temporal bandwidth in creating the traps would be needed. The effective response time of the LCoS SLM was estimated through experiments to be in the hundredths of milliseconds, which is orders of magnitude too slow. It has been demonstrated that with a faster LCoS device and special techniques a response time of as low as 1 ms can be reached [32], being a significant improvement but not enough for the purpose. One other spatial light modulator for creating dynamic trapping potential would be the acousto-optic deflector. In past works, rise times in the $\mu$s range have been achieved, making it a viable option for dynamic potential ramps [33]. Further work could therefore investigate whether an AOD can reproduce the required single-well to tilted-double-well transition while providing the necessary temporal resolution.

Overall, while the investigated LCoS SLM is suitable for the creating of static tweezers arrays, a much faster modulation technique would be required for the dynamic trapping potentials sought after in the RuPo experiment.

# Use of generative AI

Google Gemini [34] and ChatGPT [35] assisted in writing Python code for tasks such as generating plots or controlling the camera for example.
Quillbot [36] and ChatGPT [35] were used to check for grammar and spelling errors.
ChatGPT was also used in some cases to find relevant literature.

All AI suggestions were thoroughly reviewed before implementation.

# References


[1] Accessed: 30-08-2026. Kirchhoff Institute for Physics. URL: https://www.kip.uni-heidelberg.de/oberthaler/research/sopa.

[2] Eric A. Cornell and Carl E. Wieman. "Bose–Einstein Condensation in a Dilute Gas: The First 70 Years and some Recent Experiments (Nobel Lecture)". In: *ChemPhysChem* 3.6 (2002), pp. 476–493. DOI: 10.1002/1439-7641(20020617)3:6<476::AID-CPHC476>3.0.CO;2-V. URL: https://chemistry-europe.onlinelibrary.wiley.com/doi/abs/10.1002/1439-7641%2820020617%293%3A6%3C476%3A%3AAID-CPHC476%3E3.0.CO%3B2-V.

[3] T. Rick Perche, Francesco Gozzini, and Markus K. Oberthaler. *Bose polarons as relativistic Unruh-DeWitt detectors: Entanglement harvesting from Bose-Einstein condensates*. 2026. arXiv: 2512.21381 [quant-ph]. URL: https://arxiv.org/abs/2512.21381.

[4] Z. Zhang, Zheng You, and Daping Chu. "Fundamentals of Phase-Only Liquid Crystal on Silicon (LCOS) Devices". In: *Light: Science & Applications* 3, e213 (2014). DOI: 10.1038/lsa.2014.94. URL: https://www.nature.com/articles/lsa201494.

[5] Silvia Bergamini et al. "Holographic generation of microtrap arrays for single atoms by use of a programmable phase modulator". In: *Journal of the Optical Society of America B* 21.11 (2004), pp. 1889–1894. DOI: 10.1364/JOSAB.21.001889.

[6] F. Nogrette et al. "Single-Atom Trapping in Holographic 2D Arrays of Microtraps with Arbitrary Geometries". In: *Phys. Rev. X* 4 (2 May 2014), p. 021034. DOI: 10.1103/PhysRevX.4.021034. URL: https://link.aps.org/doi/10.1103/PhysRevX.4.021034.

[7] Daniel Barredo et al. "Synthetic three-dimensional atomic structures assembled atom by atom". In: *Nature* 561.7721 (2018), pp. 79–82. DOI: 10.1038/s41586-018-0450-2. URL: https://doi.org/10.1038/s41586-018-0450-2.

[8] Y. T. Chew et al. "Ultraprecise holographic optical tweezer array". In: *Physical Review A* 110.5 (Nov. 2024). ISSN: 2469-9934. DOI: 10.1103/physreva.110.053518. URL: http://dx.doi.org/10.1103/PhysRevA.110.053518.

[9] Rudolf Grimm, Matthias Weidemüller, and Yurii B. Ovchinnikov. *Optical dipole traps for neutral atoms*. 1999. arXiv: physics/9902072 [physics.atom-ph]. URL: https://arxiv.org/abs/physics/9902072.

[10] Giuseppe Pesce et al. "Optical tweezers: theory and practice". In: *The European Physical Journal Plus* 135 (Dec. 2020). DOI: 10.1140/epjp/s13360-020-00843-5.

[11] Accessed: 30-08-2026. URL: https://publish.obsidian.md/myquantumwell/Electromagnetism/Optics/Gaussian+beam#beam+radius.

[12] Thomas Hewitt et al. "Controlling the interactions in a cold atom quantum impurity system". In: *Quantum Science and Technology* 9.3 (May 2024), p. 035039. DOI: 10.1088/2058-9565/ad4c91. URL: https://doi.org/10.1088/2058-9565/ad4c91.

[13] Nikolaus Lorenz et al. "Raman sideband cooling in optical tweezer arrays for Rydberg dressing". In: *SciPost Phys.* 10 (2021), p. 052. DOI: 10.21468/SciPostPhys.10.3.052. URL: https://scipost.org/10.21468/SciPostPhys.10.3.052.

[14] Chengyu Fang et al. "Silicon-On-Sapphire Metasurfaces Generate Arrays of Dark and Bright Traps for Neutral Atoms". In: *ACS Photonics* 13.16 (July 2026), pp. 4870–4877. ISSN: 2330-4022. DOI: 10.1021/acsphotonics.6c01311. eprint: https://pubs.acs.org/apchd5/article-pdf/13/16/4870/65793361/acsphotonics.6c01311.pdf. URL: https://doi.org/10.1021/acsphotonics.6c01311.

[15] Guillaume Gauthier et al. "Chapter One - Dynamic high-resolution optical trapping of ultracold atoms". In: ed. by Louis F. Dimauro, Hélène Perrin, and Susanne F. Yelin. Vol. 70. Advances In Atomic, Molecular, and Optical Physics. Academic Press, 2021, pp. 1–101. DOI: 10.1016/bs.aamop.2021.04.001. URL: https://www.sciencedirect.com/science/article/pii/S1049250X2100001X.

[16] Michael J. Stephen and Joseph P. Straley. "Physics of liquid crystals". In: *Rev. Mod. Phys.* 46 (4 Oct. 1974), pp. 617–704. DOI: 10.1103/RevModPhys.46.617. URL: https://link.aps.org/doi/10.1103/RevModPhys.46.617.

[17] Qian Chen et al. "Complex phase modulation of liquid crystal devices with deep learning". In: *Opt. Express* 32.15 (July 2024), pp. 25883–25891. DOI: 10.1364/OE.532208. URL: https://opg.optica.org/oe/abstract.cfm?URI=oe-32-15-25883.

[18] *SLM-300 Operation Manual*. 9.0. Document version 9.0. Santec. 2019. URL: https://aoc.santec.com/en/support/usermanuals/slm/.

[19] Hao Zhang et al. "Elimination of a zero-order beam induced by a pixelated spatial light modulator for holographic projection". In: *Appl. Opt.* 48.30 (Oct. 2009), pp. 5834–5841. DOI: 10.1364/AO.48.005834. URL: https://opg.optica.org/ao/abstract.cfm?URI=ao-48-30-5834.

[20] A. He and C. Quan. "Wavefront correction for spatial nonuniformity of the liquid crystal on silicon based spatial light modulator". In: *Optics and Lasers in Engineering* 121 (2019), pp. 377–388. ISSN: 0143-8166. DOI: 10.1016/j.optlaseng.2019.05.010. URL: https://www.sciencedirect.com/science/article/pii/S0143816619300090.

[21] Carol López-Quesada, Jordi Andilla, and Estela Martín-Badosa. "Correction of aberration in holographic optical tweezers using a Shack-Hartmann sensor". In: *Appl. Opt.* 48.6 (Feb. 2009), pp. 1084–1090. DOI: 10.1364/AO.48.001084.

[22] Yansheng Liang et al. "Aberration correction in holographic optical tweezers using a high-order optical vortex". In: *Applied Optics* 57.13 (May 2018), pp. 3618–3623. DOI: 10.1364/AO.57.003618.

[23] Joseph W. Goodman. *Introduction to Fourier Optics*. 2nd ed. New York: McGraw-Hill, 1996. ISBN: 978-0-07-024254-8.

[24] Accessed: 31-09-2026. URL: https://www.newport.com/n/determination-blaze-wavelength.

[25] L. A. Romero and M. S. Millan. "Programmable Diffractive Optical Elements with Applicability in Ophthalmic Optics". In: *Optica Pura y Aplicada* 50.1 (Mar. 2017), pp. 75–91. DOI: 10.7149/opa.50.1.49509. URL: http://dx.doi.org/10.7149/OPA.50.1.49509.

[26] R. W. Gerchberg. "A practical algorithm for the determination of phase from image and diffraction plane pictures". In: *Optik* 35 (1972), pp. 237–246. URL: https://api.semanticscholar.org/CorpusID:55691159.

[27] Hui-Chi Chen and Chau-Jern Cheng. "Holographic Optical Tweezers: Techniques and Biomedical Applications". In: *Applied Sciences* 12.20 (2022). ISSN: 2076-3417. DOI: 10.3390/app122010244. URL: https://www.mdpi.com/2076-3417/12/20/10244.

[28] A. Lizana et al. "Influence of the incident angle in the performance of Liquid Crystal on Silicon displays". In: *Opt. Express* 17.10 (May 2009), pp. 8491–8505. DOI: 10.1364/OE.17.008491. URL: https://opg.optica.org/oe/abstract.cfm?URI=oe-17-10-8491.

[29] Alexander Franzen. Accessed: 1-09-2026. URL: https://www.gwoptics.org/ComponentLibrary/.

[30] Emiliano Ronzitti et al. "LCoS nematic SLM characterization and modeling for diffraction efficiency optimization, zero and ghost orders suppression". In: *Optics Express* 20 (July 2012), pp. 17843–17855. DOI: 10.1364/OE.20.017843.

[31] E Martín-Badosa et al. "Design strategies for optimizing holographic optical tweezers set-ups". In: *Journal of Optics A: Pure and Applied Optics* 9.8 (2007), S267–S277. ISSN: 1741-3567. DOI: 10.1088/1464-4258/9/8/s22. URL: http://dx.doi.org/10.1088/1464-4258/9/8/S22.

[32] Gregor Thalhammer et al. "Speeding up liquid crystal SLMs using overdrive with phase change reduction". In: *Opt. Express* 21.2 (Jan. 2013), pp. 1779–1797. DOI: 10.1364/OE.21.001779. URL: https://opg.optica.org/oe/abstract.cfm?URI=oe-21-2-1779.

[33] Lewis Picard and Manuel Endres. *A three-dimensional acousto-optic deflector*. Oct. 2025. DOI: 10.48550/arXiv.2510.07633.

[34] Google. *Gemini (Large Language Model)*. https://gemini.google.com. Accessed: 2026-09-06. 2024.

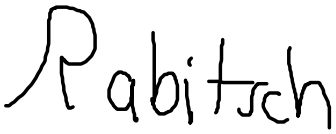
[35] OpenAI. *ChatGPT (Large Language Model)*. https://chat.openai.com. Accessed: 2026-09-06. 2024.

[36] QuillBot. *QuillBot: AI-powered writing assistant*. https://quillbot.com. Accessed: 2026-09-06. 2024.

# Erklärung

Ich versichere, dass ich diese Arbeit selbstständig verfasst und keine anderen als die angegebenen Quellen und Hilfsmittel benutzt habe.

Heidelberg, den 09.09.2026,



# Acknowledgements

Lastly, I would like to thank everyone who made this Bachelor's thesis possible.

First and foremost, I would like to thank Prof. Markus Oberthaler for giving me the opportunity to work in his research group and for supervising this thesis.

I would also like to thank Prof. Matthias Weidemüller for serving as the second examiner of this thesis.

I am very grateful to my lab mates Brian, Fabian, and Lorenz for always being available, answering my questions, and providing valuable advice throughout the writing of this thesis.

Finalamente, quiero dar las gracias a mi novia Gianna por apoyarme y estar siempre a mi lado. Yo te amo demaisado.

# Appendix A

# Wavefront correction

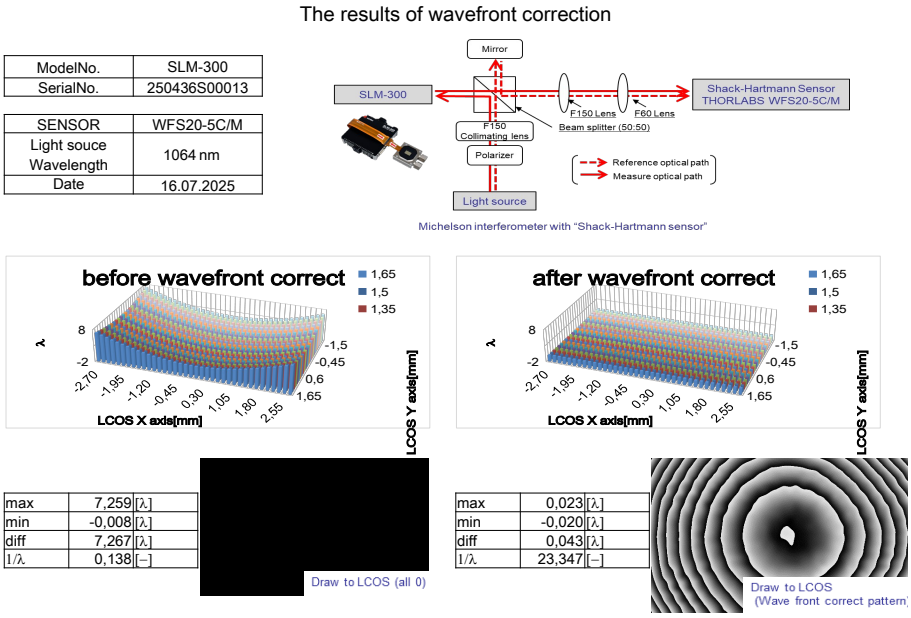



Figure A.1: Wavefront measurement provided by the manufacturer Santec for constructing the wavefront correction phase pattern found on the included USB flash drive.

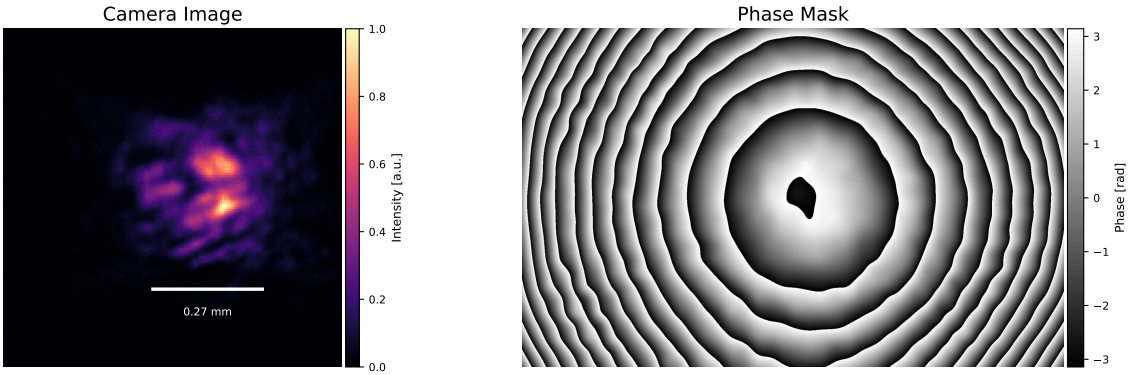



Figure A.2: Inverse wavefront correction ($-\Phi_{wf}$ from eq.2.2.3).

# Appendix B

# WGS optimization

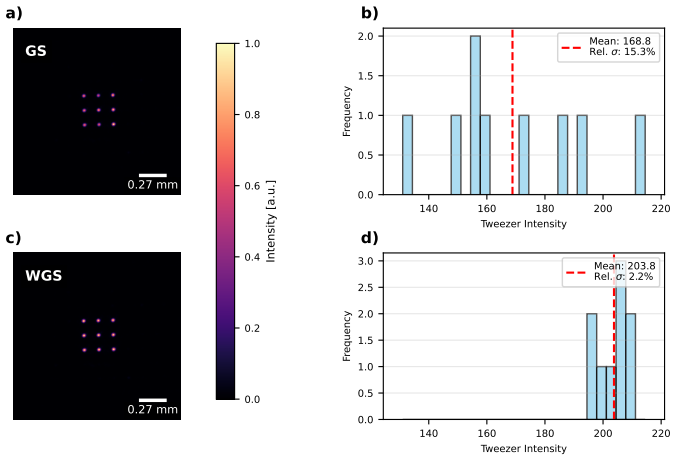



Figure B.1: Comparison of GS-algorithm created 3x3 tweezer array with that optimized by the WGS-algorithm analogous to fig.4.7

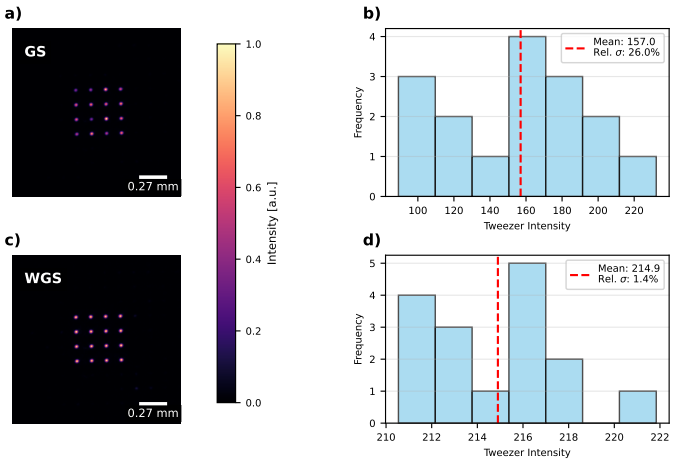



Figure B.2: Comparison of GS-algorithm created 4x4 tweezer array with that optimized by the WGS-algorithm analogous to fig.4.7

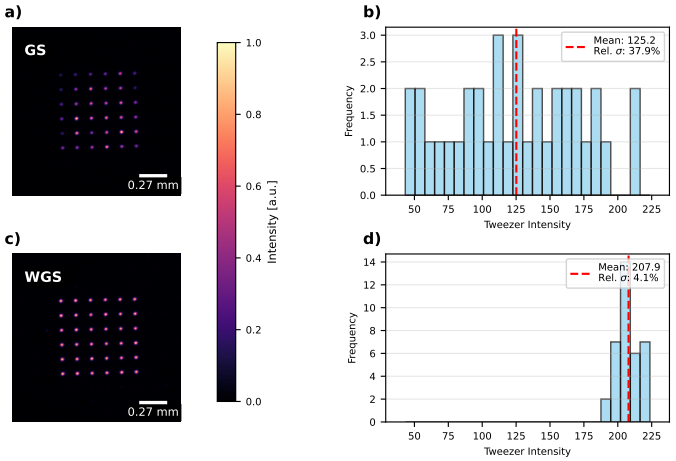



Figure B.3: Comparison of GS-algorithm created 6x6 tweezer array with that optimized by the WGS-algorithm analogous to fig.4.7

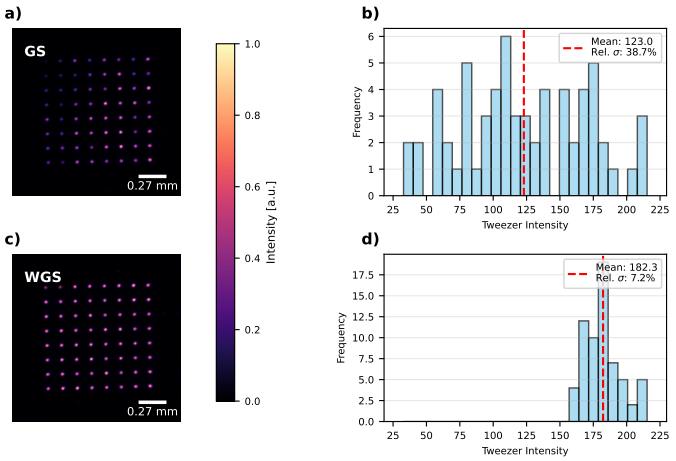



Figure B.4: Comparison of GS-algorithm created 8x8 tweezer array with that optimized by the WGS-algorithm analogous to fig.4.7

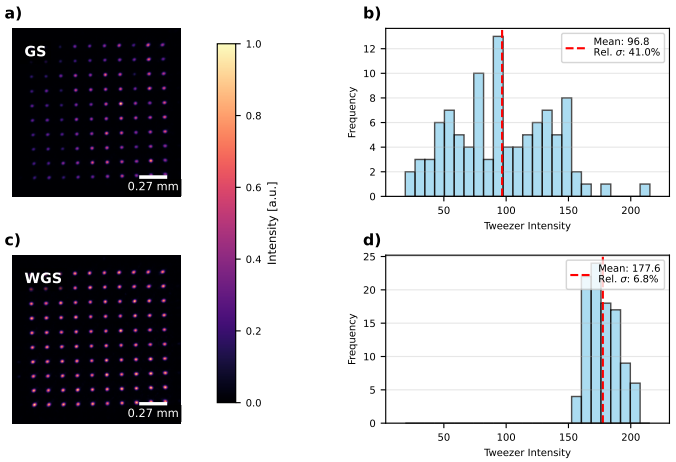



Figure B.5: Comparison of GS-algorithm created 10x10 tweezer array with that optimized by the WGS-algorithm analogous to fig.4.7